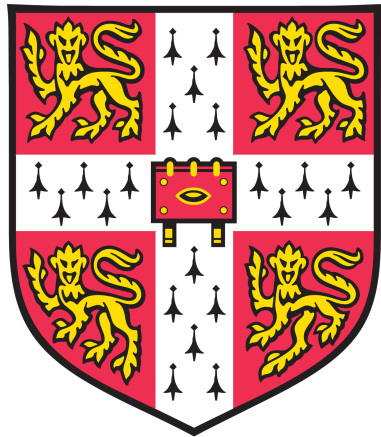


UNIVERSITY OF CAMBRIDGE
DEPARTMENT OF ENGINEERING

MASTERS PROJECT REPORT



Propulsion Systems for VTOL Electric Vehicles

Jordan Sandberg Eriksen

SUPERVISED BY: Dr Sam Grimshaw

Abstract

Abstract here..

Contents

1	Introduction	1
1.1	Measuring Propulsor Performance	1
1.1.1	Figure of Merit	1
1.1.2	The Superiority Condition	3
1.1.3	Design Point	5
1.1.4	Design Context	5
1.2	Literature Review	5
1.3	Research Question	5
1.4	Approach	6
2	Flying Test Bed System Design	6
2.1	Flying Test Bed	6
2.1.1	Mechanical design	6
2.1.2	Customisation of <i>Pixhawk 4</i> flight hardware/software	7
2.1.3	Subsystem Functions	8
2.1.4	Subsystem Interaction	9
2.1.5	Telemetry	9
3	Ducted Fan Aerodynamic Design	10
3.1	Introduction	10
3.2	Mean-line Design	10
3.2.1	Non-dimensional Operating Point:	11
3.2.2	Fan Operating Speed:	12
3.2.3	Mean-line Location:	12
3.2.4	Overall Performance	12
3.2.5	Mass Model	13
3.2.6	Design Selection	15
3.3	3D Blade Design	18
3.3.1	3-dimensional Flow Solutions to Radial Equilibrium:	18
3.3.2	3D Velocity Triangles:	20
3.3.3	Validation of Mean-line Location:	21
3.3.4	Blade Number and Span-wise Chord:	22
3.3.5	Deviation	24
3.3.6	Blade Lean	25
3.3.7	Noise	25
3.3.8	Blade Profiles	25
3.3.9	Blade Generation	26

4 Electrical and Mechanical Design	26
4.1 Introduction	26
4.2 Electrical Design	26
4.2.1 Motor Requirements	26
4.2.2 Power Supply	26
4.2.3 Choice of Electric Motor	27
4.3 Mechanical Design	27
4.3.1 Propulsor Dimensions	28
4.3.2 Shrouded Rotor	28
4.3.3 Stator Block: Stator Blades, Casing, and Hub	30
4.3.4 Diffuser	31
4.3.5 Intake	31
4.3.6 3D Printing	32
5 Experimental Methods	32
5.1 Cage Design & Tether	32
5.2 Stationary Propulsor Test	32
5.2.1 Setup	33
5.3 Hover Test	35
5.3.1 Setup	35
5.3.2 Control	36
5.4 Measurement Techniques	36
5.4.1 Non-dimensional Quantities	36
5.4.2 Data Acquisition and Processing	38
6 Results	39
6.1 Stationary Propulsor Test	39
6.1.1 System and Electrical Efficiency	40
6.1.2 Ducted Fan Figure of Merit (<i>Version 3.1</i>)	41
6.1.3 Ducted Fan Mass Model – ΔW	44
6.1.4 Superiority Condition	44
6.1.5 Intake Performance (<i>Version 1.0 EDF</i>)	45
6.1.6 Diffuser Performance (<i>Version 2.0 EDF</i>)	45
6.1.7 Vortex Design (<i>Version 2.0 EDF</i>)	45
6.2 Hover Tests	46
6.2.1 Propeller Performance	46
6.2.2 Hover Test Limitations	46
7 Future Work	47
7.1 Propulsor Design	47
7.1.1 Exploration of the Superiority Condition	47
7.1.2 Contra-rotating Ducted Fan (CRDF)	47
7.1.3 Computational Fluid Dynamics (CFD)	48

7.2	Stationary Propulsor Experiments	49
7.3	Flying Test Bed Experiments	50
7.3.1	Static Hover Test Adaptations	50
7.3.2	Manoeuvre Tests	50
8	Conclusions	51

Nomenclature

e-VTOL	Test
FTB	Test
V_x	Axial flow velocity
Ω	
r_h	
r_c	
r_m	
U	
ϕ	Flow coefficient
ψ	Stage loading

1 Introduction

Vertical take-off and landing (VTOL) electric vehicles are becoming a more sought after solution to human transportation needs than ever before, yet the unshrouded propeller is still the most common propulsion system on the market. It can easily be shown that the addition of a shroud, or duct, can significantly improve the thrust generated at a given power or reduce the power required to maintain a given thrust. The ducted fan is the logical evolution of the propeller. Current VTOL electric vehicles are limited by the weight and the energy density of batteries. In order to carry enough energy for practical journeys to be made a large number of battery cells must also be transported, meaning propulsion systems are larger and require more power, requiring more batteries... The use of ducted fans reduces the power requirement from the propulsion system and therefore increases range. Furthermore the casing provides rotor containment in the case on an emergency and can provide stowage for batteries and other systems to increase payload space and reduce structural stresses. However, the high thrust to weight ratio of the propeller means vehicle weight is hardly affected. This is not the case with a ducted fan, requiring considerably more blades, a hub structure, an intake duct, a casing, and an exit duct. The question arises as to whether this increase in weight can be overcome by a ducted fan's higher performance, but this question is very subjective and it's answer dependent on the application being designed for – the resulting design space for a ducted fan is therefore vast and multi-dimensional highlighting the multi-disciplinary nature of the problem.

This report consolidates these variables and presents a simple condition by which the performance of two candidate propulsors for an application can be compared. This condition is applied to the design of a ducted fan that aims to perform better than a VTOL optimised propeller when carrying a specified load. The condition is also used to explore the design space and suggest which applications could benefit from the use of ducted fans.

1.1 Measuring Propulsor Performance

Good performance in hover is achieved by maximising the thrust to weight ratio of a propulsor. Being in hover means the thrust generated must be equal to the vehicle weight and so good performance becomes maximising the weight to power ratio. Power requirement is inherently reliant on the weight of the vehicle and so this relationship must also be explored.

1.1.1 Figure of Merit

The effectiveness of a propulsor in hover can be measured by the figure of merit, M_F , defined as a non-dimensional thrust-to-power ratio

$$M_F = \frac{T}{P} \sqrt{\frac{T}{2\rho A_x}} \quad (1.1)$$

where A_x , the blade passage axial flow area, can be related to the exit duct exit area, A_e , by the area ratio

$$\sigma = \frac{A_e}{A_x} \quad (1.2)$$

Considering the large control volume around the ducted fan in Fig. 1, the thrust generated by the fan can be determined from the steady flow momentum equation (SFME). Assuming zero inlet swirl and straight and parallel exit flow (zero exit swirl), the static pressure at the duct exit, p_e , is equal to atmospheric pressure, p_a . Continuity gives the relationship between duct exit velocity and area ratio

$$\dot{m} = \rho A_x V_x = \rho A_e V_e \quad \therefore \sigma = \frac{V_x}{V_e} \quad (1.3)$$

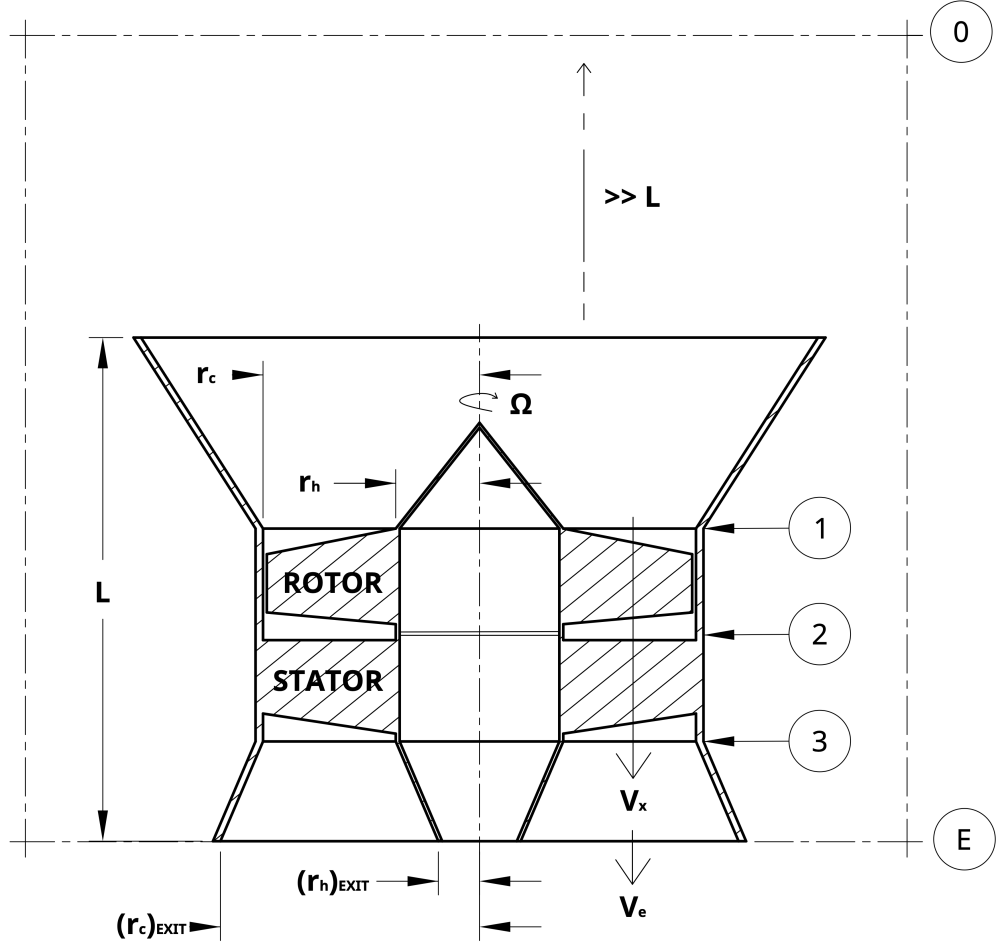


Figure 1: Ducted fan configuration and control volume. **0**: Control volume inlet plane; **1**: Rotor inlet plane; **2**: Inter-rotor-stator plane; **3**: Stator exit plane; **E**: Exit duct/control volume exit plane.

Therefore the SFME can be written in terms of the blade passage quantities (A_x and V_x) and the area ratio, σ

$$T = \dot{m}V_e \quad \therefore T = \frac{\rho A_x V_x^2}{\sigma} \quad (1.4)$$

Flow power is determined from the steady flow energy equation (SFEE)

$$P = \frac{1}{2}\dot{m}V_e^2 \quad \therefore P = \frac{\rho A_x V_x^3}{2\sigma^2} \quad (1.5)$$

Substituting Eqn. 1.4 and Eqn. 1.5 into Eqn. 1.1 gives a simplified expression for figure of merit of a ducted fan

$$M_F = \sqrt{2\sigma} \quad (1.6)$$

Therefore ducting the fan with an area ratio of $\sigma = 1$ gives a figure of merit of $M_F = \sqrt{2}$. Pereira (2008)[1] shows the maximum figure of merit for a propeller to be 1. Provided the area ratio of the exit duct on a ducted fan remains $\sigma > 0.5$ the ducted fan figure of merit is greater.

1.1.2 The Superiority Condition

Although figure of merit characterises propulsor performance in static hover it doesn't consider the extra propulsor weight associated with a ducted fan – due to casing, intake, and diffuser – and the associated increase in required thrust. Therefore to equate the performance of a propeller and a ducted fan the power required to maintain hover with the same payload must be equal. As propulsor and associated control system weight varies with design and application, the payload capacity relative to the propulsor weight must be considered. The propeller performance is taken as the datum case. The power required for the propeller to maintain static hover – where the propulsor thrust is equal to the vehicle weight/ N_P (where N_P is the number of propulsors) – is calculated from the shaft figure of merit (calculated using shaft power) and the vehicle weight, W .

$$P = \frac{W/N_P}{(M_{F,s})_{prop.}} \sqrt{\frac{W/N_P}{2\rho A_{x,prop.}}} \quad (1.7)$$

Using the same power, the thrust obtainable with the ducted fan can be found by rearranging Eqn. 1.1

$$T_{fan} = \left[(M_{F,s})_{fan} P \sqrt{2\rho A_{x,fan}} \right]^{\frac{2}{3}} \quad (1.8)$$

Equation 1.8 is a significant result. For a given application, in order to perform better than a propeller, the thrust developed with the same power input must be greater than the new total vehicle weight. Expressing total thrust requirement in terms of the original vehicle weight and the extra weight due to the ducted fans gives

$$N_P \cdot T_{fan} \geq W \left(1 + \frac{\Delta W}{W} \right) \quad (1.9)$$

where ΔW is the extra weight of the vehicle due to the ducted fans. Combining Eqn. 1.8 and Eqn. 1.9 gives

$$W \left(1 + \frac{\Delta W}{W} \right) \leq N_P \left[(M_{F,s})_{fan} P \sqrt{2\rho A_{x,fan}} \right]^{\frac{2}{3}} \quad (1.10)$$

Using the thrust = weight condition satisfied by the propeller in Eqn 1.7, this can be rewritten as

$$W \left(1 + \frac{\Delta W}{W} \right) \leq \left[\frac{(M_{F,s})_{fan} \sqrt{A_{x,fan}}}{(M_{F,s})_{prop.} \sqrt{A_{x,prop.}}} \right]^{\frac{2}{3}} \cdot N_P \left[(M_{F,s})_{prop.} P \sqrt{2\rho A_{x,prop.}} \right]^{\frac{2}{3}} \quad (1.11)$$

Hence the requirement for the ducted fan to perform better than the propeller is

$$1 + \frac{\Delta W}{W} \leq \left[\frac{(M_{F,s})_{fan} \sqrt{A_{x,fan}}}{(M_{F,s})_{prop.} \sqrt{A_{x,prop.}}} \right]^{\frac{2}{3}} \quad (1.12)$$

Taking the theoretical figure of merit for the fan ($M_{F,s} = \sqrt{2\sigma}$) and propeller ($M_{F,s} = 1$), and given that $\Delta W = W_{fan,total} - W_{prop,total}$ this becomes simply

$$\frac{W_{fan,total}}{W_{prop.total}} \leq \left[2\sigma \frac{A_{x,fan}}{A_{x,prop.}} \right]^{\frac{1}{3}} \quad (1.13)$$

Eqn. 1.13 provides two explicit design objectives:

1. Exit duct exit area must be maximised ($A_e = \sigma A_x$);
2. Propulsor weight must be minimised

Clearly there is a conflict here as an increase in flow area will increase propulsor size and weight. Furthermore increasing exit duct area ratio above 1 means the exit is now a diffuser. To prevent the flow in a diffuser from separating the length of diffuser required will scale with the exit duct area ratio. In order to determine how this inequality can be satisfied the relationship between the geometric quantities on the RHS (σ and A_x) and the resulting propulsor weight must be found. This is achieved by creating a mass model that estimates the weight of the propulsor of given size and operating point, A_x and σ respectively. The inequality in Eqn. 1.13 is referred to here as a superiority condition as any design that satisfies this condition will require less (or equal) power to maintain hover than an ideal propeller of a specified size and hence have superior performance.

1.1.3 Design Point

Both Eqn. 1.6 and Eqn. 1.13 suggest the performance of a ducted fan can be determined using 3 variables; exit duct area ratio σ , fan radius r_c and fan hub-to-tip ratio HTR (assuming annular fan area A_x is defined as $\pi r_c^2(1 - HTR^2)$). Multiple fan designs may satisfy the above criteria but with varying efficiencies. The fan design space must therefore be explored further.

1.1.4 Design Context

The ducted fans considered here are restricted by available manufacturing techniques. This introduces physical limits on the maximum size of propulsor that can be manufactured and tested. Ducted fans are to be 3D printed and so the size of the build plate limits the maximum outer diameter of the propulsor. The length of any cylindrical components is also limited by the vertical travel of the build plate. The propulsor must therefore be designed within these limits. Given a fixed payload (defined by the weight of the flying test bed chassis) Eqn. 1.13 could be satisfied provided a large enough fan can be produced. This requirement is explored in the design section as the limiting size for the superiority condition to be satisfied can only be determined once a suitable mass model is developed.

1.2 Literature Review

Considerable work on ducted fans has been conducted since the 1930s and there has been an rise in research in the field in recent years due to the increasing interest in personal aerial vehicles (PAVs) as well as unmanned aerial vehicles (UAVs). Zhang et al. (2020)[2] presents the state of the art in ducted fan research and should be referred to for a full survey of open-domain published works. Importantly it fails to identify significant research into ducted fan performance based on turbomachinery theory and instead all analysis focuses on propeller theory (considering advance ratio as opposed to flow coefficient, for example). Furthermore the design space is not considered in the context of a specific application and instead considers the ducted fan in isolation. This must be considered in order to quantify performance for a given application.

1.3 Research Question

A simple question is proposed for this project:

Are ducted fans more efficient than propellers in hover?

The size of this design space highlights the importance of a systems approach to the problem and therefore its multi-disciplinary nature. This question is broken down into 4 sub-questions.

1. Can an exit duct exit area ratio greater than 1 and a corresponding figure of merit greater than $\sqrt{2}$ be achieved?

2. For a specific application and design context can the superiority condition be satisfied?
3. Does performance in-flight reflect predicted performance from stationary tests?

This requires a suitable platform be developed to enable comparison of in-flight and stationary performance, as well as provide the context and application required for the ducted fan design process.

1.4 Approach

The design of a flying test bed system is described to enable both stationary tests and hover tests of a variety of propulsors. The aerodynamic design of a ducted fan is then considered. Overall performance is determined by considering the 2-dimensional mean-line design, followed by the 3-dimensional design. The design objective is to require less power to maintain static hover than a propeller driven vehicle. The final aerodynamic design is then embodied and the electrical and mechanical aspects of the design are considered. First a VTOL optimised propeller with known performance is tested on a stationary rig to calibrate the system then the ducted fan is tested on the same rig to compare performance. The propeller is used on the flying test bed to conduct hover tests to verify the method for determining in flight performance. These tests are analysed and sources of loss and deviations from design are discussed. Finally, suggestions for further work are presented and discussed.

2 Flying Test Bed System Design

The flying test bed is a system developed to enable testing of propulsors in an application driven environment. Its roles are to manage data collection and power supply during stationary tests, and control vehicle dynamics and collect data during hover tests.

2.1 Flying Test Bed

A UROP was conducted in the summer preceding this project during which an axi-symmetric quadcopter flying test bed was designed and tested. The two challenges addressed were structural design of the chassis, and the customisation of flight control hardware and software. The UROP concluded with successful hover testing of the flying test bed. Off-the-shelf 10in. propellers were used in the test (see Fig. 2).

2.1.1 Mechanical design

The test bed was designed to be rapidly 3D printable, light weight – whilst maintaining structural integrity – and modular to allow various propulsors and instrumentation to be mounted. Instrumentation management and flight hardware are mounted on a central chassis that is 3D printed as one piece for rigidity and to reduce complexity. Cantilevered propulsor

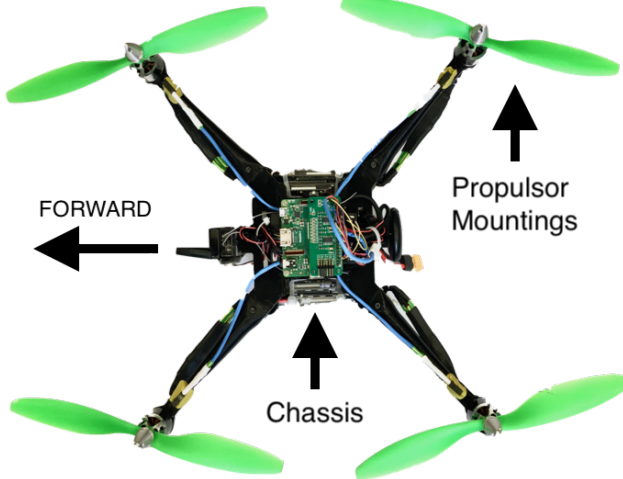


Figure 2: Image of flying test bed with propellers attached

arms are attached to the central chassis with a double mortise and tenon style mount, fastened by one M3 cap-head as in Fig. 3. Modularity allows for design iteration and rapid part replacement if required.

The following hardware is mounted directly onto the central chassis:

- ***Pixhawk 4 Flight Control hardware*** – Packaged, customizable autopilot hardware
- **PM07 Power Module** – Power module managing distribution of power from battery/power supply to flight controllers, other on-board computers, and motors
- **Raspberry Pi 3 Model A+** – On-board computer managing data acquisition and assisting flight controller automation
- **ADCPi ADC Breakout** – Analogue to digital converter mounted directly to the Raspberry Pi 3
- **4x Aerostar 50A ESC** – Electronic Speed Controller driving BLDCM motors
- **Optional: Turnigy 5000mAh 14.8V (4-cell) Battery** – Large capacity 14.8V (nominal) battery. Can be replaced by a tethered 12V power supply.

The central chassis has dimensions of approximately 125mm x 139mm x 93mm. It has a dry mass (excluding battery) of 0.529kg and the battery has a mass of 0.466kg.

2.1.2 Customisation of *Pixhawk 4* flight hardware/software

Pixhawk 4 is a packaged flight control hardware system running open source PX4 firmware. Interaction with the system is via the GUI QGroundControl and either a wireless telemetry

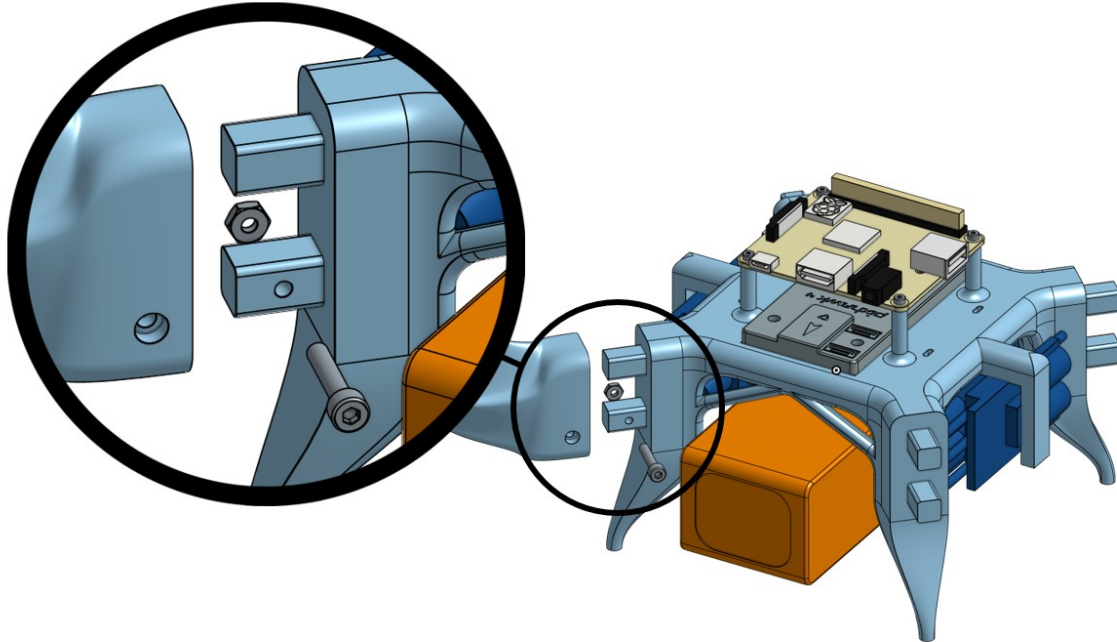


Figure 3: Flying test bed chassis showing exploded detail of double mortise and tenon joint for propulsor arms

transmitter-receiver pair or a serial connection (such as a USB). QGroundControl allows a predetermined automated flight path to be followed or alternatively the hardware can be configured to allow manual control provided adequate control inputs can be provided (a 16-channel remote with an 8-channel PPM-PWM converter is used here). The PM4 firmware includes various airframe configuration profiles, enabling it to adapt to the vehicle configuration and motor layout. The flying test bed is configured as a symmetric ‘X’ quadcopter. The profile was tuned to the flying test bed by varying PID gains on the control software, ensuring stable operation in hover. It provides a stable hover mode that is intended to reduce horizontal position deviation and maintain a fixed altitude. This means only small corrective inputs are required from the operator to ensure near stationary hover even in enclosed environments. It was found however that wall effects can be significant and so care must be taken when operating in such environments.

2.1.3 Subsystem Functions

Raspberry Pi 3 Model A+ (RPi3)

The RPi3 is a light-weight, small-footprint, 64-bit quad-core processor with UNIX-based operating system and Wi-Fi connectivity that can be run ‘blind’ through an SSH connection from a remote machine. It provides data acquisition and on-board data processing in Python and is used to pre-process test data before wirelessly transferring it back to the remote machine. RPi3 has 28 general purpose input/output (GPIO) pins as well as I²C and

serial interfaces among others.

ADCPi ADC Breakout

The ADC breakout board is designed specifically for the RPi3. Operating through the I²C interface, each breakout board provides an 8-channel ADC at 11 to 17 bit resolution with sample rates of 240 to 3.75 *samples/sec* respectively.

PM07 Power Module

Designed to operate in tandem with the Pixhawk 4 flight controller, the PM07 provides power control for all the high-power outputs (such as the motors) as well as a regulated 5V output for the flight controller and RPi3. Power input is 7-51V DC and the output current is limited to 120A (approximately 30A per propulsor). The battery selected can operate up to 125A to accommodate this demand. PM07 also provides 2 ADC inputs.

2.1.4 Subsystem Interaction

Pixhawk 4 provides simple subsystem interaction through it's input ports. 5 ports connect the flight controller to the power module: 2x power inputs, 1x motor PWM outputs, 1x auxiliary PWM output, and 1x ADC input. The serial port on the Pixhawk 4 is rewired to connect to the RPi3's UART TXD and RXD terminals. The I²C port connects to an I²C bus that allows up to 5 devices to interface with the Pixhawk 4, including 3 ultrasound sensors measuring proximity in the x, y, and z directions. These sensors can optionally be connected via the ADC for use by the RPi3. Figure 4 shows schematically how the subsystems interact.

2.1.5 Telemetry

Pixhawk 4 wireless telemetry

The plug-and-play telemetry module allows wireless connection to the Pixhawk 4 from a ground control station on a remote machine such as QGroundControl. This is used to communicate with the Pixhawk 4 about flight control and to log power usage data (PM07 voltage and current output).

SSH/SCP on RPi3

RPi3 is wireless enabled allowing it to be accessed remotely via the SSH (secure shell) protocol. SCP (secure copy protocol) allows files to be copied to and from the RPi3. This is used after data collection to collect all data on the remote machine. A dedicated wireless router is used to connect the RPi3 to a remote machine – done automatically on start-up of the RPi3.

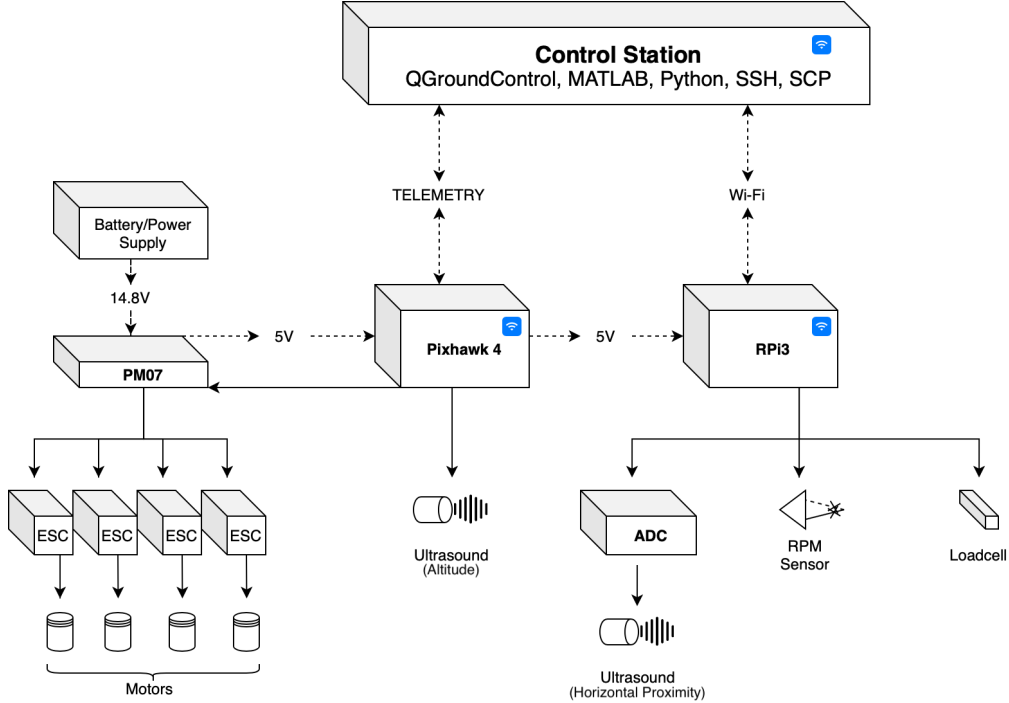


Figure 4: Subsystem schematic of flying test bed

3 Ducted Fan Aerodynamic Design

3.1 Introduction

This section describes the aerodynamic design of an electric ducted fan, 3D printed in PLA, that is designed to replace a propeller on a VTOL electric vehicle. The flying test bed is powered by 4 ducted fans and is required to be able to achieve a steady hover with a payload equal to the weight of the flying test bed. Figure 1 shows a schematic of the ducted fan configuration with labelled blade passage casing radius r_c , blade passage hub radius r_h , diffuser exit casing radius $(r_c)_{exit}$, diffuser exit hub radius $(r_h)_{exit}$, rotor angular velocity Ω , blade passage axial velocity V_x , and diffuser exit velocity V_e . The design process is summarised by the flow chart in Fig. 5. The MATLAB® design code developed to design the ducted fan follows the same flow.

3.2 Mean-line Design

The propulsor design at mean-line is described below. The choice of mean-line location for a low hub-to-tip ratio (HTR) machine is discussed and validated.

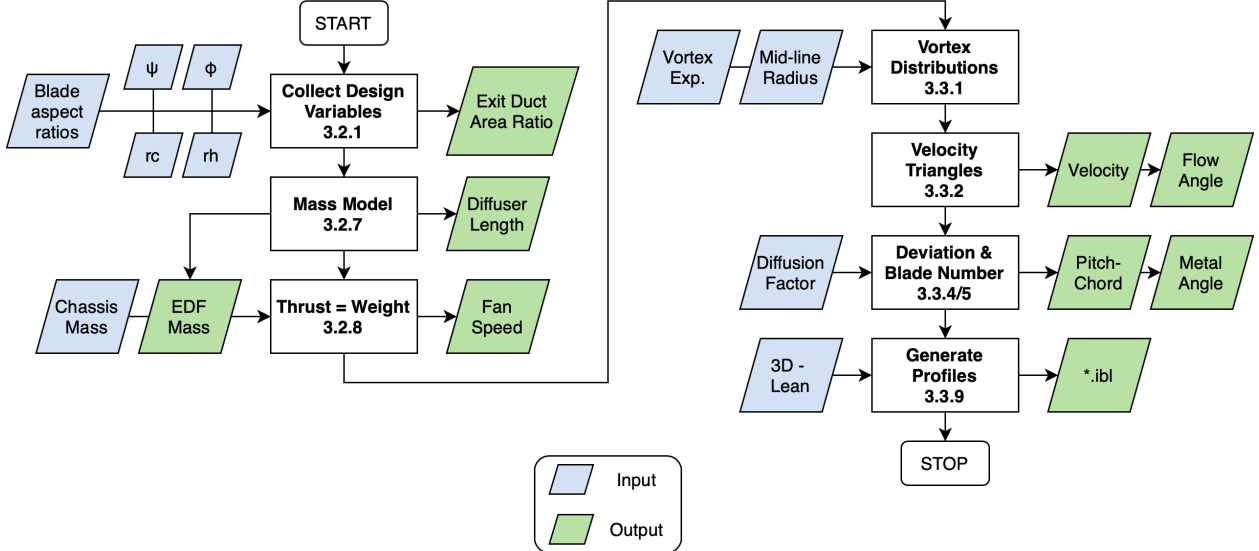


Figure 5: Flow chart showing the aerodynamic design process. 2D design stages are on the left and the 3D design stages are on the right. Processes are labelled by the report section in which they appear (3.x.x)

3.2.1 Non-dimensional Operating Point:

The design of the rotor and stator fan blades is determined by the choice of non-dimensional operating point given by flow coefficient (Eqn. 3.1a) and stage loading (Eqn. 3.1b) where the mean-line blade velocity is $U = \Omega \cdot r_m$ with r_m equal to the mean-line radius.

$$\phi = \frac{V_x}{U} \quad (a) \qquad \psi = \frac{\Delta h_0}{U^2} \quad (b) \quad (3.1)$$

Assuming isentropic flow, stage loading can be written in terms of the stagnation pressure rise, Δp_0 . Using Bernoulli and the assumption exit static pressure is equal to atmospheric gives an expression for Δh_0 in terms of axial blade passage velocity V_x and area ratio.

$$\begin{aligned} \Delta p_0 &= (p_0)_e - (p_0)_{in} = (p_e + \frac{p_a}{2} \rho V_e^2) - p_a \\ \Delta p_0 &= \frac{1}{2} \rho V_e^2 \\ \Delta h_0 &= \frac{\Delta p_0}{\rho} \end{aligned} \quad (3.2)$$

$$\Delta h_0 = \frac{V_x^2}{2\sigma^2} \qquad \therefore \psi = \frac{V_x^2}{U^2} \cdot \frac{1}{2\sigma^2} \quad (3.3)$$

Therefore ϕ , ψ , and σ are related by

$$\psi = \frac{\phi^2}{2\sigma^2} \quad (3.4)$$

The operating point can therefore be defined by the area ratio, σ and the flow coefficient, ϕ . This allows the desired figure of merit to be chosen and the required stage loading to be found.

3.2.2 Fan Operating Speed:

Equation 1.6 shows that the figure of merit for a ducted fan in hover is independent of the speed of rotation of the fan. The fan speed, however, impacts the magnitude of thrust developed, shown by substituting Eqn. 3.1(a) into Eqn. 1.4.

$$T = \frac{\rho A_x (\Omega r_m \phi_m)^2}{\sigma} \quad (3.5)$$

This shows thrust to vary with both fan speed and fan size, and so the required thrust will vary depending on the choice of these parameters. The effect of fan size is discussed in section 3.2.

3.2.3 Mean-line Location:

Maximising the flow area for a given propulsor radius maximises thrust developed (Eqn. 3.5) and ensures minimum use of material and therefore a lighter design. This results in a small hub radius (limited only by electric motor size, typically $\approx 20mm$) and consequently low hub-to-tip ratios (< 0.5). Selecting a mean-line at the midspan radius gives different mass flows above and below the mean-line and this results in variation in loading across the span. An alternative mean-line position is defined by balancing the mass flow above and below the mean-line. This sets the mean-line radius at the root-mean-square of the hub and tip radii

$$r_m = \sqrt{\frac{r_h^2 + r_c^2}{2}} \quad (3.6)$$

3.2.4 Overall Performance

The expressions for fan thrust and power can now be determined in terms of the non-dimensional operating point and the fan's geometric variables as in Eqn. 3.7 and Eqn. 3.8.

$$T = \frac{\rho \pi \phi_m^2 \Omega^2 (r_c^4 - r_h^4)}{2\sigma} \quad (3.7)$$

$$P = \frac{\rho \pi \phi_m^3 \Omega^3 (r_c^2 - r_h^2)}{2\sigma^2} \left(\frac{r_c^2 + r_h^2}{2} \right)^{\frac{3}{2}} \quad (3.8)$$

3.2.5 Mass Model

In order to solve the superiority condition a mass model is required to relate estimated propulsor weight to design variables σ , r_c , and r_h . Figure 6 shows an exploded view of the components making up the mass model. The diffuser hub and casing, and the intake are modelled as hollow truncated cones. The blade duct hub and casing are modelled as hollow cylinders. Blade rows are modelled as thin annular disks.

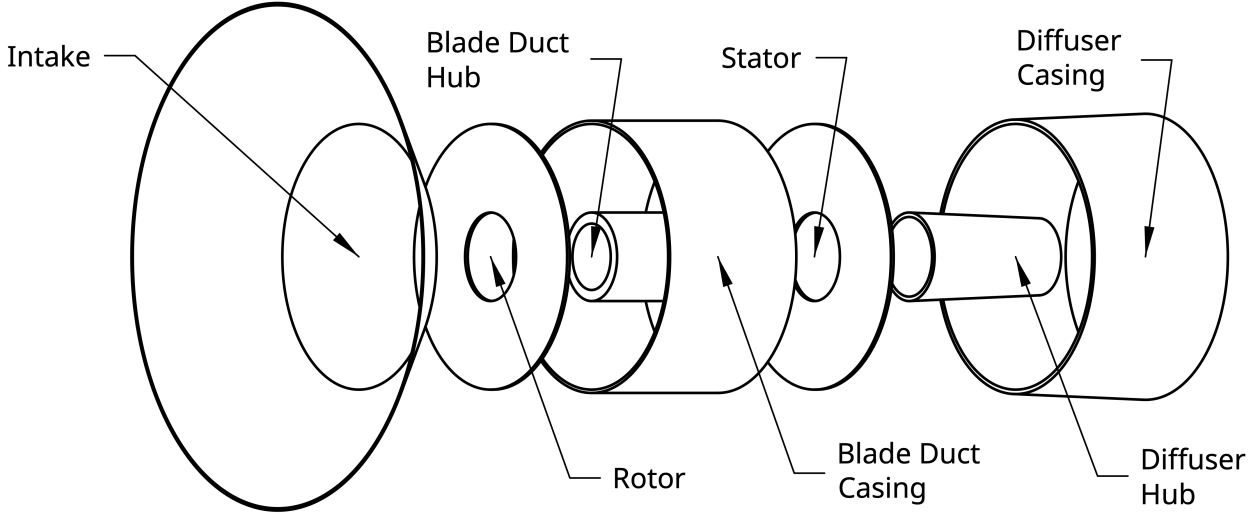


Figure 6: Exploded view of ducted fan mass model components

Diffuser: ESDU 75026[3] presents the performance of symmetric annular diffusers in incompressible flow. The length of diffuser required to prevent separation is estimated from Fig. 32 in Appendix D which gives empirical limits of separation at various length and area ratios for symmetric annular diffusers. Considering Eqn. 1.3 and Bernoulli's equation, static pressure recovery can be written as

$$C_{pr} = \frac{p_e - p_x}{\frac{1}{2}\rho V_x^2} = 1 - \frac{1}{\sigma^2} \quad (3.9)$$

Figure 32 shows two limit lines, C_{pr}^* and C_{pr}^{**} representing the separation limit and the limit of performance due to frictional loss and boundary layer growth respectively. Designing on the appropriate constant C_{pr} line close to C_{pr}^{**} will produce a diffuser that is unlikely to separate. This line can be approximated with an R-squared value of 0.9999 by

$$\frac{L_{diff.}}{r_c - r_h} = -5.56\sigma^3 + 24.16\sigma^2 - 23.41\sigma + 5.413 \quad (3.10)$$

The diffuser hub and casing are modelled as hollow truncated cones with height $L_{diff.}$ (determined by Eqn. 3.10), a base radius r_h (for the hub) and $(r_c)_{exit}$ (for the casing), a truncation radius of $(r_h)_{exit}$ (for the hub) and r_c for the casing, and a thickness t , as in Fig. 1.

Diffuser exit hub and casing radius for a symmetric diffuser can be found by considering the equal flow angle at the hub and casing giving

$$\frac{(r_c)_{exit} - r_c}{L} = \frac{r_h - (r_h)_{exit}}{L} \quad (3.11)$$

$$\therefore (r_c)_{exit}, (r_h)_{exit} = \frac{r_c + r_h}{2} \pm \frac{\sigma}{2}(r_c - r_h) \quad (3.12)$$

	Hub value	Casing value
R	r_h	$(r_c)_{exit} + t$
r	$(r_h)_{exit}$	$r_c + t$
S	$r_h - t$	$(r_c)_{exit}$
s	$(r_h)_{exit} - t$	r_c
h	$L_{diff.}$	$L_{diff.}$

Table 1: Parameter values for diffuser hub and casing

Equation 3.13 gives the volume of a hollow truncated cone using the variables defined in Table. 1 allowing the total mass of the diffuser to be determined.

$$V = \frac{h\pi}{3}(R^2 + Rr + r^2 - S^2 - Ss - s^2) \quad (3.13)$$

$$m_{diff.} = \rho_{PLA}(V_{hub} + V_{case}) \quad (3.14)$$

Blade Passage: The blade passage (excluding rotor and stator) are modelled as a straight annulus 3D printed in PLA. The passage itself has inner radius r_h and outer radius r_c . The casing is modelled to have thickness of $t_c = 1.5mm$ and the hub section has a thickness of $t_h = 5mm$. The length of the blade passage is $L_{BP} = 70mm$ giving a total mass of

$$m_{BP} = \rho_{PLA}L_{BP}\pi[2r_ht_h - t_h^2 + 2r_ct_c + t_c^2] = 2.73r_h + 0.818r_c - 0.0062 \quad (3.15)$$

Intake: For simplicity the intake is also modelled as a hollow truncated cone, an approximation for it's actual ellipsoidal geometry. It has approximately equal length to it's change in radius which is set approximately equal to the blade passage span, $r_c - r_h$. Therefore using Eqn. 3.13, and assuming a thickness of $1mm$, the intake mass can be approximated by

$$m_{in.} = 3.90(r_c - r_h)(3r_c - r_h + 0.001) \quad (3.16)$$

Blades: As the number of blades has not yet been determined, the blades are modelled as having the equivalent mass of a annular flat disk of thickness $t_{rotor} = 1.5mm$ for the rotor and $t_{stator} = 1.5mm$ for the stator. The resulting mass is given by

$$m_{blades} = \rho_{PLA} \pi (r_c^2 - r_h^2) (t_{rotor} + t_{stator}) \quad (3.17)$$

$$m_{blades} = 11.7(r_c^2 - r_h^2) \quad (3.18)$$

Thrust–Weight Balance: The mass model described above provides an approximation for the mass of a particular design. In hover, the load carried by each propulsor is equal to the propulsor weight and its share of the payload weight (4 propulsors). The payload here is the flying test bed chassis and battery, described in section 2.1. Using Eqn. 3.7 the thrust developed can be set equal to the required thrust to give the relationship between the design variables when the propulsor is operating in the static hover state.

$$T = g \left[m_{fan} + \frac{m_{chassis}}{4} + \frac{m_{battery}}{4} \right] \quad (3.19)$$

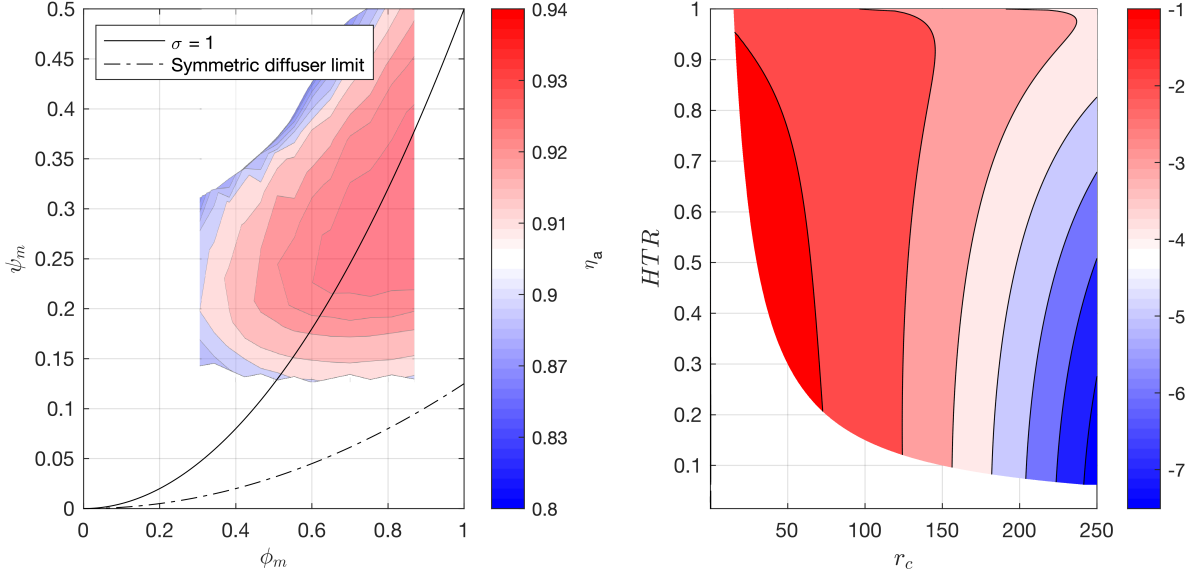
$$\frac{\rho \pi \phi_m^2 \Omega^2 (r_c^4 - r_h^4)}{2\sigma} = g[m_{diff.} + m_{BP} + m_{in.} + m_{blades}] + 2.44N \quad (3.20)$$

3.2.6 Design Selection

The following constraints are objectives are imposed on the design space. They are considered in the following order.

1. Design in a high efficiency region for low Reynolds number blades
 - Choose operating point for ϕ and ψ , hence determine σ
2. Satisfy the superiority condition (Eqn. 1.13)
 - Minimise propulsor mass
 - Maximise flow area and exit duct area ratio
 - Choose geometric design point for r_c and HTR
3. Operate in a suitable speed-torque regime for the electric motor
 - Calculate operating point for Ω based on T , σ , and ϕ as in Eqn. 3.5

Blade Operating Point: Figure 7a shows a smith chart for the Maffioli et al. (2015)[4] low Reynolds number blade profiles used in this design overlaid on the ϕ_m - ψ_m design space. It shows blade efficiency in a 2D cascade to decrease for flow coefficients $\phi_m < 0.6$ and stage loading $\psi_m < 0.2$. This is verified by Corralejo and Harley (2017)[5]. The design region also has an upper limit of $\sigma = 1$ as well as a lower symmetric diffuser limit, arising from the diffuser hub converging to a point. The design region is also limited by the $\eta_a = 0.95$ contour. The operating point of $\phi_m = 0.8$, $\psi_m = 0.25$ is chosen as it lies in the middle of



(a) Blade operating point design space shown with exit duct area ratio limits and Maffioli et al. (2015)[4] Smith chart overlaid. Note non-linear color bar

(b) Superiority condition across the r_c - HTR geometric design space. Missing corner represents designs with a hub radius of $r_h < 15\text{mm}$

Figure 7: Blade aerodynamic and propulsor geometric design spaces

this design region. This gives an exit duct area ratio of $\sigma = 1.1314$.

Geometric Design Point: Using the mass model the superiority condition is determined in terms of the free variables r_c , HTR and the value of $\sigma = 1.1314$ from Eqn. 1.13. As discussed in Section 1.1.4 the maximum size of the propulsor is limited by manufacturing methods. The minimum hub radius is determined by the size of the electric motor (typically $r_h > 15\text{mm}$) and so the design space explored is defined by $15\text{mm} \leq r_c \leq 250\text{mm}$ and a HTR range of $0 \rightarrow 1$ (provided $r_h > 15\text{mm}$). It is found that for the flying test bed chassis payload, no combination of r_c and HTR satisfy the superiority condition. Figure 7b shows the value of the difference between the RHS and LHS of the superiority condition to be negative throughout the design region. The nearest design region to satisfying the condition is at low values of r_c and low values of HTR . Hence a casing radius of 60mm and a HTR of 1/3 is chosen, giving a hub radius of 20mm.

Electric Motor Operating Point: The mass model is used to estimate the weight of the ducted fan propelled vehicle and therefore determine the thrust required ($T = Wg/N_P$). Equation 3.7 is used to calculate the rotor speed required to achieve this thrust

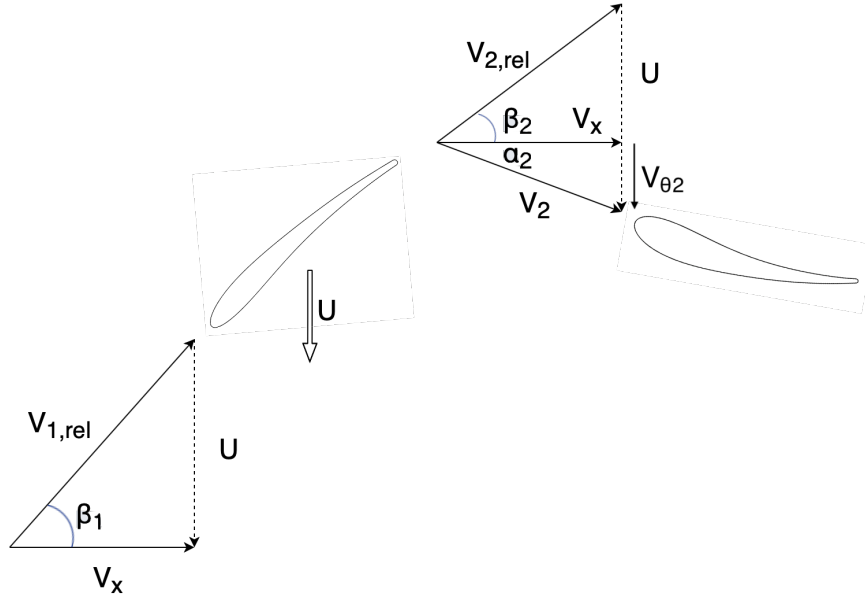


Figure 8: Mean-line velocity triangles (stator exit omitted as flow axial at exit)

$$\Omega = \sqrt{\frac{2\sigma \frac{Wg}{N_p}}{\rho \pi \phi_m^2 (r_c^4 - r_h^4)}} \quad (3.21)$$

$$\therefore \Omega = 627.5 \text{ rad} \cdot \text{s}^{-1} = 5992 \text{ RPM} \approx 6000 \text{ RPM} \quad (3.22)$$

ϕ_m	0.80
ψ_m	0.25
σ	1.1314
$L_{diff.}$	72.0 mm
r_c	60 mm
r_h	20 mm
r_m	44.7 mm (RMS)
Ω	6000 RPM

Table 2: Propulsor design point

Velocity Triangles: Now the design parameters have been determined the mean-line velocity triangles can be drawn for this particular design. Figure 8 shows the velocity triangles in context with rotor and stator blades. Flow angles are measured positive in the sense of rotor rotation (in Fig. 8 positive down).

3.3 3D Blade Design

Overall performance has been determined by setting the mean-line values of flow coefficient, ϕ_m , and stage loading, ψ_m . The values of ϕ and ψ must vary along the span as the local value of blade speed changes, and for equilibrium to be maintained across the flow passage. In order to satisfy these conditions the radial equilibrium equation must be satisfied. Potential solutions to this equation are discussed below.

3.3.1 3-dimensional Flow Solutions to Radial Equilibrium:

Radial equilibrium states that for axi-symmetric and incompressible annulus flow Eqn. 3.23 must be satisfied.

$$\frac{dh_0}{dr} - T \frac{ds}{dr} = V_x \frac{dV_x}{dr} + \frac{V_\theta}{r} \frac{d(rV_\theta)}{dr} \quad (3.23)$$

Assuming there is no variation in stagnation enthalpy or entropy across the span, this reduces to

$$V_x \frac{dV_x}{dr} + \frac{V_\theta}{r} \frac{d(rV_\theta)}{dr} = 0 \quad (3.24)$$

Noting Eqn. 3.1 and applying Euler's work equation, we obtain

$$\phi r \frac{d(\phi r)}{dr} + \psi \frac{d(\psi r^2)}{dr} = 0 \quad (3.25)$$

Which has general solutions in the form

$$\phi = \phi_m \left(\frac{r}{r_m} \right)^A \quad (a) \qquad \psi = \psi_m \left(\frac{r}{r_m} \right)^B \quad (b) \quad (3.26)$$

where ϕ_m and ψ_m are the mean-line quantities. Substituting eqns.3.26a & 3.26b into Eqn. 3.25 gives

$$\begin{aligned} \left[\phi_m \left(\frac{r}{r_m} \right)^A \right]^2 (1 + A) &= - \left[\psi_m \left(\frac{r}{r_m} \right)^B \right]^2 (2 + B) \\ \therefore \phi^2 (1 + A) &= -\psi^2 (2 + B) \end{aligned} \quad (3.27)$$

This solution can be used to determine the values of the exponents, A and B . The constant B is referred to here as the vortex distribution exponent as it determines the tangential velocity variation in the r - θ plane.

Free Vortex ($B = -2$): One such distribution arises from the free vortex condition. This results from the solution to Eqn. 3.27 in which both LHS and RHS are equal to zero giving

$$A = -1 \quad (a) \qquad B = -2 \quad (b) \quad (3.28)$$

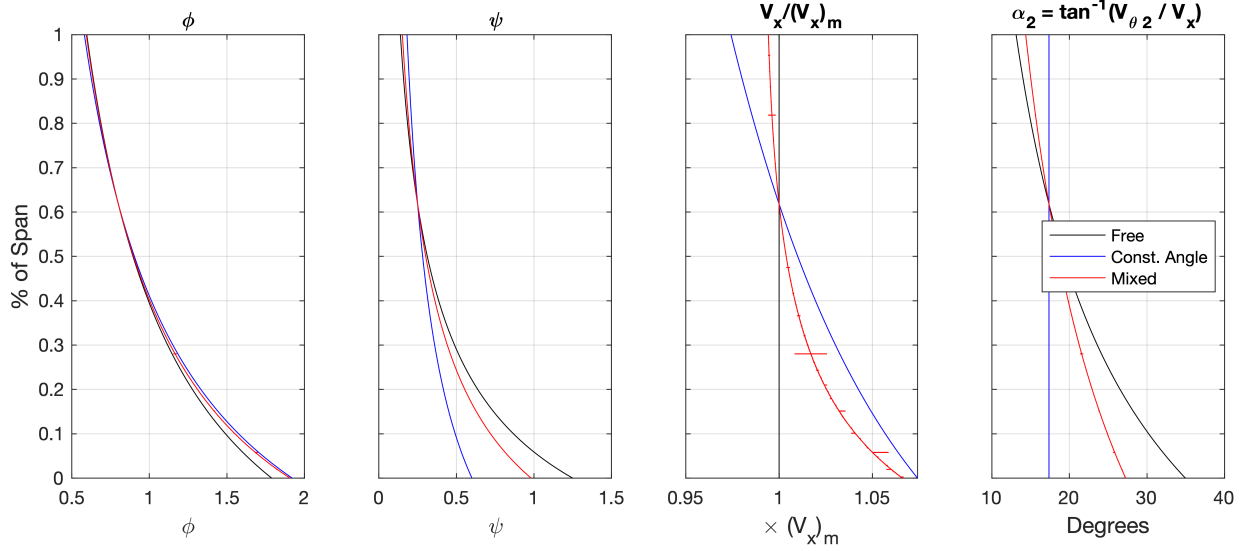


Figure 9: Distributions of design parameters ϕ and ψ and non-dimensionalised axial and tangential velocities, V_x and $V_{\theta 2}$ respectively, across the span at 3 different boundary conditions (free vortex, constant angle and mixed vortex).

Therefore from Eqn. 3.26a and Eqn. 3.28a

$$\phi(r) \sim \frac{1}{r} \quad \therefore \frac{d}{dr}(V_x) = 0 \quad (3.29)$$

Therefore axial velocity across the span must be constant. Similarly it can be shown from Eqn. 3.26b and Eqn. 3.28b

$$\psi(r) \sim \frac{1}{r^2} \quad \therefore \frac{d}{dr}(\Delta h_0) = 0 \quad (3.30)$$

Therefore the loading is equal across the span. It can then be determined that $V_{\theta 2} \sim 1/r$ resulting in a vorticity free (lowest loss) flow[6]. Both the constant V_x and the constant Δh_0 conditions indicate uniform exit static pressure. In practice the variation in $V_{\theta 2}$ across the span results in large variations in blade twist angle that should be avoided (see Fig. 9 that shows $V_{\theta 2}$ variation resulting in over 20° of absolute flow angle variation). Furthermore, Fig. 9 shows stage loading, ψ , to become larger than 1 at radii close to the hub. From Euler, and given axial inlet flow

$$\Delta V_\theta = V_{\theta 2} = \psi U \quad (3.31)$$

This shows the tangential velocity at the hub to be greater than the local blade speed. By reducing the value of the vortex distribution exponent, B , this can be avoided by keeping $\psi_{hub} \leq 1$.

Mixed Vortex ($-2 \leq B \leq 0$): Equation 3.27 can also be used to numerically solve the radial equilibrium equation for any value of the vortex distribution exponent provided ϕ_m and ψ_m are known. A summary of vortex distribution exponent values is shown in tab. 3. The mixed vortex design shown in Fig. 9 has a vortex distribution exponent of -1.7 . This produces a vortex distribution that, at the hub, has a tangential velocity equal to the velocity of the hub wall. This reduces the absolute velocity of the flow past the wall and therefore minimises frictional loss at the hub. Hereafter any reference to a ‘mixed vortex condition’ corresponds to a vortex distribution exponent of $B = -1.7$, as described here.

Constant Angle: Another common design is for constant absolute flow angle across the span, such that

$$\frac{d}{dr} \left(\frac{V_\theta}{V_x} \right) = 0 \quad (3.32)$$

$$\therefore \frac{\psi}{\phi} = \text{constant} \left(= \frac{\psi_m}{\phi_m} \right) \quad (3.33)$$

This results in the exponents A and B being equal giving

$$A = B = - \left(\frac{2\psi_m^2 + \phi_m^2}{\psi_m^2 + \phi_m^2} \right) \quad (3.34)$$

	Free Vortex $V_x(r) = \text{const.}$	Constant Angle $V_x/V_\theta = \text{const.}$	$B = \dots$ see Eqn. 3.27
A	-1	$-\left(\frac{2\psi_m^2 + \phi_m^2}{\psi_m^2 + \phi_m^2}\right)$	<i>Solve numerically</i>
B	-2	$-\left(\frac{2\psi_m^2 + \phi_m^2}{\psi_m^2 + \phi_m^2}\right)$	<i>Solve numerically</i>

Table 3: Vortex distribution exponents for various boundary conditions

3.3.2 3D Velocity Triangles:

Once the distributions of ϕ and ψ have been determined the variation in flow velocities and angles can be found across the span. The value of any velocity or angle can be found using the appropriate local values of the spanwise variables ϕ , ψ , U , and r . The relative merits

of each of the vortex distributions are discussed in Section ?? in which the three designs presented here are tested.

3.3.3 Validation of Mean-line Location:

Eqn. 3.7 and Eqn. 3.8 come from the assumption that mean-line design parameters are representative of the performance of the whole flow. This assumption can be verified now that the span-wise distribution of the flow parameters has been determined. Integrating the work done and thrust generated by an infinitesimal annulus element allows the real power and thrust produced by the propulsor to be determined. This is computed numerically and the expression obtained above for each of the parameters in Eqn. 3.37.

$$P = \int_{r_h}^{r_c} \Delta h_0 \cdot d\dot{m} \quad (3.35)$$

$$\Delta h_0 = \psi U^2 \quad (a) \quad d\dot{m} = \rho V_x (2\pi r dr) \quad (b) \quad (3.36)$$

$$\therefore P = 2\pi\rho\Omega^3 \cdot \frac{\phi_m \psi_m}{r_m^{B+A}} \int_{r_h}^{r_c} r^{A+B+3} dr \quad (3.37)$$

A similar expression can be obtained for the thrust developed. The mass-averaged mean-line radius definition of r_m is compared to the conventional mean-line radius definition of r_m in Table 4 by calculating the error between the real power and thrust and the predicted one obtained from Eqn. 3.8 and Eqn. 3.7. A properly balance mean-line radius choice will ensure the real power is as close to the predicted one as possible, minimising this error

Mean-line radius	P error	T error
$r_m = \text{mean}(r_c, r_h)$	37%	24%
$r_m = RMS(r_c, r_h)$	1.2%	0.36%

Table 4: Comparison of power and thrust from predicted (from constant mean-line parameters) and real (from integral of span-wise distributions) using various mean-line definitions

Table 4 shows the selection of a mean-line radius at the RMS of the hub and casing radius reduces the error between the real and the predicted power requirements to $\approx 1\%$. These errors are small enough to be neglected and so this choice of mean-line radius is validated.

Vortex Design	Diffusion Factor	N_R	Selected	N_S	Selected
Free Vortex	$DF = 0.45$	(5.60)	7	(4.66)	5
	$0.25 \leq DF \leq 0.4$	(10.48)	11	(7.20)	7
Mixed Vortex	$DF = 0.45$	(5.60)	7	(4.66)	5
	$0.25 \leq DF \leq 0.4$	(10.48)	11	(7.20)	7

Table 5: Rotor and stator blade numbers at various design conditions

3.3.4 Blade Number and Span-wise Chord:

Lieblein et al. (1953)[7] present a correlation for diffusion factor as a function of velocities and the pitch-chord ratio of the blades.

$$DF = \left(1 - \frac{V_{2,rel}}{V_{1,rel}}\right) + \left(\frac{V_{\theta 1,rel} - V_{\theta 2,rel}}{2V_{1,rel}}\right) \frac{s}{c} \quad (3.38)$$

Given that the change in tangential flow velocity is the same in both the absolute and the rotor relative reference frames, and the inlet flow is axial, this becomes

$$DF = \left(1 - \frac{V_{2,rel}}{V_{1,rel}}\right) + \left(\frac{V_{\theta 2}}{2V_{1,rel}}\right) \frac{s}{c} \quad (3.39)$$

This expression is valid for both the rotor and stator provided the relative values are taken in the respective blade's frame off reference. Having determined the span-wise variation in the flow velocities and angles in Section *3D Velocity Triangle* above, the value of the local pitch-chord ratio, s/c , can be found provided a suitable diffusion factor is chosen. Consider first a constant value of diffusion factor that lies below the separation limit suggested in CUED Turbomachinery I¹ as $DF_{lim} = 0.6$, such as $DF = 0.45$. Pitch-chord across the span can be determined as

$$\frac{s}{c} = \left[DF - \left(1 - \frac{V_{2,rel}}{V_{1,rel}}\right)\right] \left(\frac{2V_{1,rel}}{V_{\theta 2}}\right) \quad (3.40)$$

In order to determine span-wise pitch, the number of blades are determined using the mean-line values. The mean-line chord is estimated using the blade mean-line aspect ratio

¹reference handout

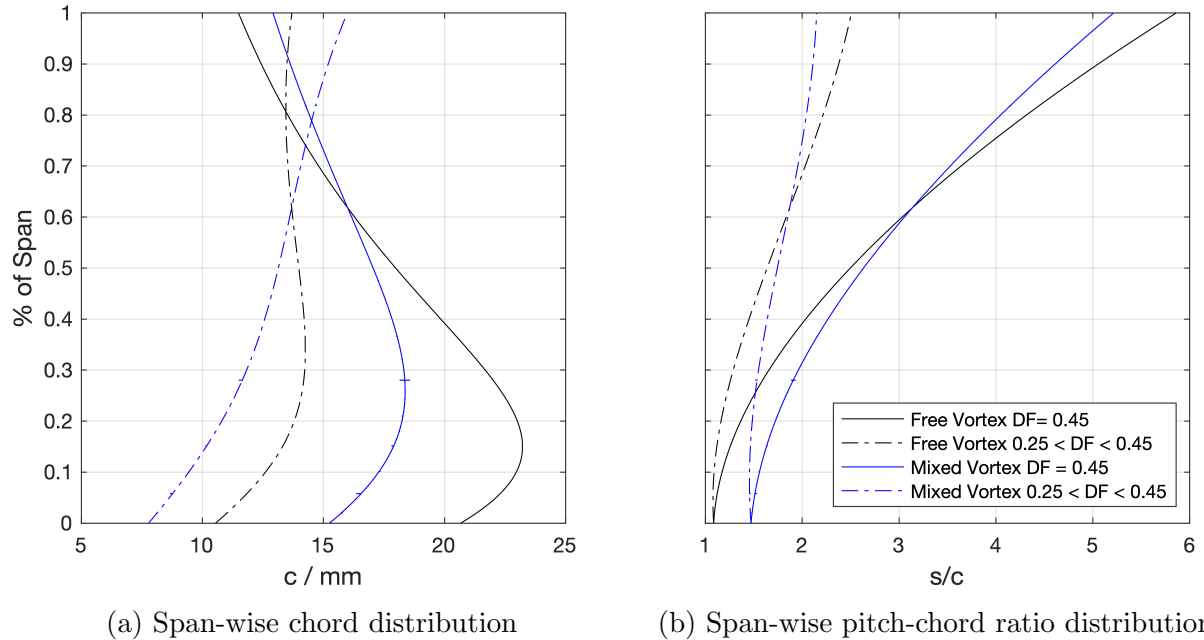


Figure 10: Span-wise distributions are shown for both the free and mixed vortex conditions (black and blue lines respectively). Each is also shown with a constant value of diffusion factor ($DF = 0.45$, solid line) and varying diffusion factor linearly across the span ($DF_{hub} = 0.45$; $DF_{tip} = 0.25$, dot-dashed line)

where $AR = \text{span}/\text{chord} = l/c$

$$c_m = \frac{r_c - r_h}{AR} \quad (3.41)$$

$$N = \frac{2\pi r_m}{(s/c)_m c_m} \quad (3.42)$$

The blade number is rounded up to the next integer value. Table 5 at the end of this section (*Blade Number and Span-wise Chord*) outlines the calculated and selected blade numbers for each of the designs discussed. Using the blade number the local chord can be determined using local pitch-chord ratio and radius such that

$$c = \frac{2\pi r}{(s/c)N} \quad (3.43)$$

The resulting span-wise chord distribution from both the free and mixed vortex conditions are shown in Fig. 10a (solid line). For the free vortex condition it shows the variation in chord across the span to be large with the tip chord is less than half the maximum chord. Changing to the mixed vortex condition reduces this variation significantly with both the tip chord increasing and the hub chord decreasing. The variation in the free vortex design

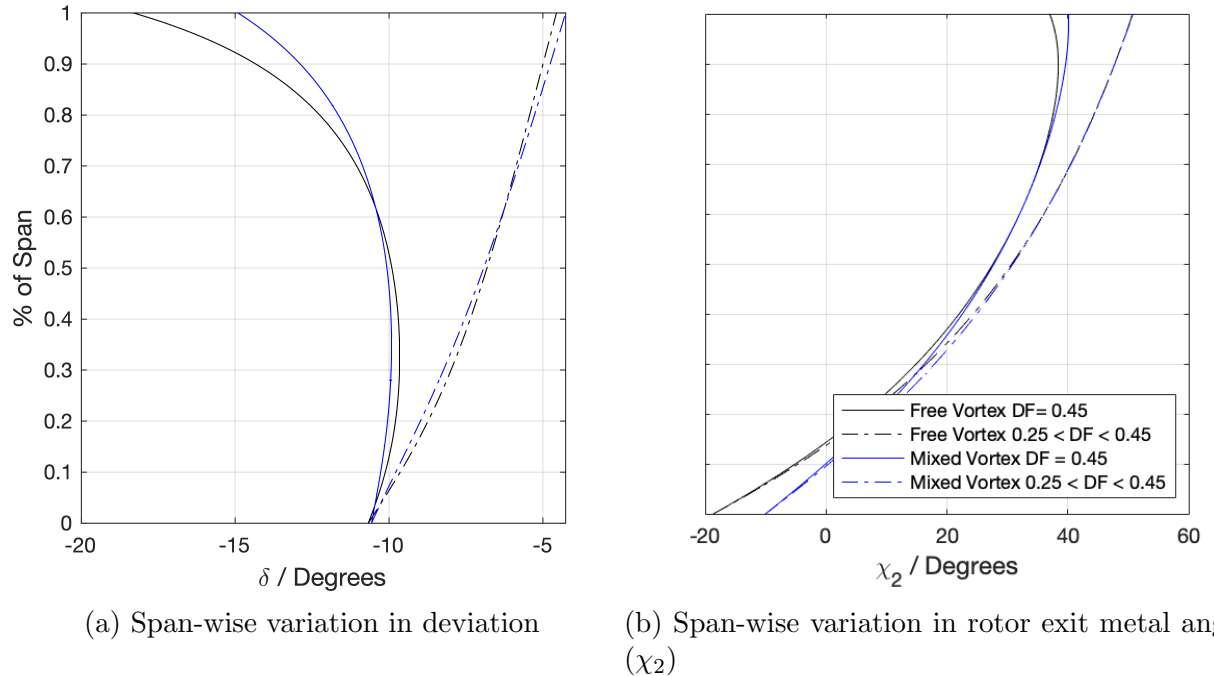


Figure 11: Span-wise distributions are shown for both the free and mixed vortex conditions (black and blue lines respectively). Each is also shown with a constant value of diffusion factor ($DF = 0.45$, solid line) and varying diffusion factor linearly across the span ($DF_{hub} = 0.4$; $DF_{TIP} = 0.25$, dot-dashed line)

arises from Eqn. 3.40 as the range of velocities across the span result in large variations in pitch-chord ratio (as in Fig. 10b).

Lieblein et al. (1953)[7] shows the increase in loss for diffusion factors above 0.55 in the hub to mean-line regions, and 0.3 in the tip region. Therefore varying the diffusion factor across the span reduces the losses due to high diffusion factor and maintains a constant margin to Lieblein's suggested limits. The dot-dashed lines in Fig. 10b show the same operating point as the solid lines but with the diffusion factor varying linearly from 0.4 at the hub to 0.25 at the tip. This limits the variation in pitch-chord ratio across the span.

Consistency in pitch-chord has further implications for deviation and is explored in the following section.

3.3.5 Deviation

Flow deviation is estimated from correlations proposed by Howell (1945)[8], (1945)[9], and Carter (1950)[10]. Commonly referred to as Carter's rule it states that for a compressor blade

$$\delta = m\theta \sqrt{\frac{s}{c}} \quad (3.44)$$

where θ is the flow turning achieved in the relative frame, and m is an empirically determined variable that can be approximated by

$$m = 0.23 \left(\frac{2a}{l} \right)^2 + \frac{\beta_2}{500} \quad (3.45)$$

where for a circular arc camber line $a/l = 0.5$. Hence the deviation varies $\sim \sqrt{s/c}$. Figure 11a shows the large increase in deviation angle at the rotor tips for both the free and the mixed vortex conditions when a constant diffusion factor is used (solid lines). Introducing a varying diffusion factor (dot-dashed lines) across the span reduces this deviation as the pitch-chord ratio varies less across the span (Fig. 10b). Carter's rule is derived from empirical results obtained from compressor cascades (hub-tip ratio ≈ 1), and as such care must be taken when applying it to blades with large span-wise variations in pitch-chord ratio. A varying diffusion factor reduces the range of pitch-chord ratio significantly and Carter's rule predicts lower deviation angles. Consequently the variation in rotor exit metal angle is more consistent, as in Fig. 11b.

3.3.6 Blade Lean

Taylor (2016)[11] shows the limits of using a 2-dimensional design with respect to 3-dimensional flow. Ensuring the blade suction surface subtends the hub and casing at an obtuse angle helps reduce corner separations and trailing edge losses. Lean is added to the rotor and stator blades to satisfy this requirement. The rotor has 10° of lean at the hub and approximately 40° at the tip and the stator follows a parabolic lean profile with 10° of lean at the hub and tip.

3.3.7 Noise

Similar blade numbers in the rotor and stator or low common multiples of blade number will result in more blade interaction and therefore higher acoustic dB. If possible, odd or prime numbers are selected to minimise interaction, provided this number is not too far from the calculated value. Table 5 shows the number of blades calculated for each design and the number of blades selected.

3.3.8 Blade Profiles

Low Reynolds number blade profiles were obtained from Maffioli et al. (2015)[4]. The profile is designed for $Re \approx 5 \times 10^4$.

3.3.9 Blade Generation

The design flowchart in Fig. 5 is constructed in a MATLAB design environment to produce blade profiles as *.ibl files that are imported into a CAD package to begin the propulsor mechanical design.

4 Electrical and Mechanical Design

4.1 Introduction

With the propulsor design specified the electrical and mechanical design must be considered. The electric motor and corresponding power supply is chosen to be compatible with both the propulsor aerodynamic design and the system control and instrumentation architecture. The aerodynamic design discussed above is embodied into a 3D printable propulsor. Geometric deviations from design are considered and minimised.

4.2 Electrical Design

4.2.1 Motor Requirements

Required motor speed is 6000 RPM giving a required power of 54.4 W. The shaft torque required can therefore be found from $P = T_s \cdot \Omega \implies T_s = 0.0867 \text{Nm}$. This is the flow torque required for lossless flow assuming no windage and electrical losses from the motor, or other frictional losses. The delay between a vehicle disturbance and the motors responding to this disturbance, known as the control latency, must also be minimised to increase stability. Reducing the control latency also reduces data noise when conducting hover tests as the power requirement from the motors is more stable. Therefore, the motors must possess sufficient torque to rapidly respond to the control system. The moment of inertia of the rotor about its rotation axis is $I_{ZZ} = 51.01 \text{kg} \cdot \text{mm}^2$ from a mass analysis of a CAD model of the rotor. The angular acceleration of the rotor is given by

$$I_{ZZ}\dot{\Omega} + \frac{T_s}{\eta_a} = T_m \quad (4.1)$$

where η_a is the aerodynamic efficiency. Taking the flow torque as constant and equal to the value obtained above, the required motor torque, T_m for a given angular acceleration of the shaft is equal to

$$T_m = 51.1 \times 10^{-6} \cdot \dot{\Omega} + \frac{0.0867}{\eta_a} \quad (4.2)$$

4.2.2 Power Supply

A 12V/84A (1kW) DC power supply is used to power the stationary propulsor tests and can be used in conjunction with a tether to provide flight power for hover tests. The flying test

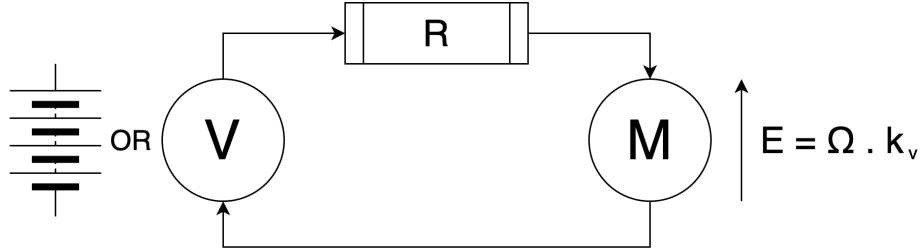


Figure 12: Electric motor model for DC/BLDC motors

bed is also equipped to hold a 4-cell Li-Po with a nominal voltage of 14.8V to enable future dynamic testing. The 12V power supply is used to determine the motor requirements as it is the limiting factor.

4.2.3 Choice of Electric Motor

A brushless DC motor (BLDCM) is modelled by the circuit in Fig. 12. The back-emf generated by the motor is proportional to the motor speed (as in Fig. 12) and the torque produced is proportional to the current. Given that the torque constant and emf constant are related by $k_t = 1/k_v \implies T_m = 3k_t I_{phase} = \frac{\sqrt{3}I_{supply}}{k_v}$. The motor speed can be related to the electrical input quantities by

$$V = IR + E \implies V = \left(\frac{T_m k_v}{\sqrt{3}} \right) R + \Omega k_v \quad (4.3)$$

$$\therefore \Omega = \left(V - \frac{T_m k_v}{\sqrt{3}} R \right) \cdot k_v \quad (4.4)$$

Assuming linear acceleration from rest to demand speed (a_{max}) and a maximum acceleration time of 75ms, Eqn. 4.2 gives a maximum motor torque requirement of $T_m = 0.428 + 0.0867/\eta_a$ Nm. The motor is required to have an outer diameter no greater than 30mm to fit inside the hub with hub wall thickness of 5mm. These requirements, are met by a Multistar Elite 2810-750kv BLDCM with internal resistance of 0.108 ohms and emf constant of 750 $RPM \cdot V^{-1}$. Rearranging Eqn. 4.4 gives an output torque at operating speed of

$$T_m = 0.76 Nm \quad (4.5)$$

Allowing for an aerodynamic efficiency of $\eta_a \approx 30\%$ whilst accelerating at a_{max} .

4.3 Mechanical Design

In this section the propulsor design is embodied and the mechanical aspects of the design considered. For hover testing the propulsors positioned diagonally opposite from each other spin in one sense and those on the other diagonal spin in the other sense. This gives the

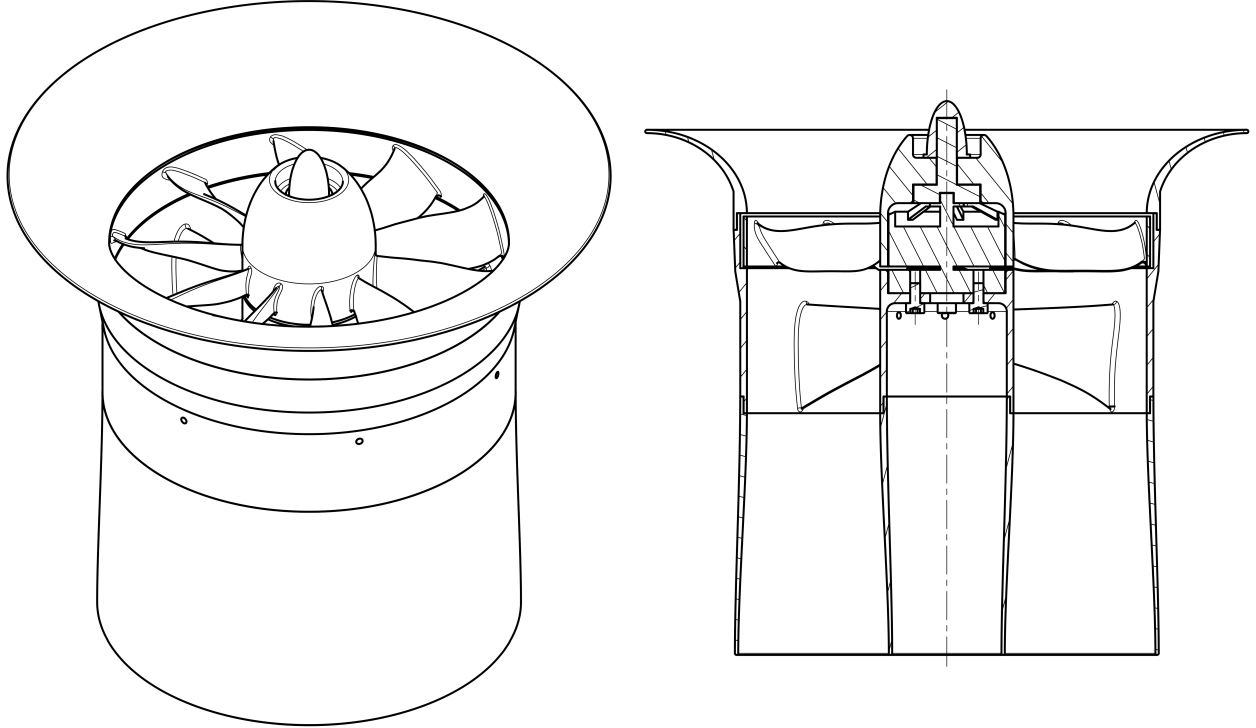


Figure 13: Isometric and section view of ducted fan design

flying test bed yaw control. As a result two versions of the propulsor are produced, one spinning clockwise and the other anti-clockwise. These are simple mirror images of each other and so need not be discussed further.

4.3.1 Propulsor Dimensions

The rotor and stator profiles determined in Section 3.3 have a total axial chord of 52.5mm including a 12mm blade row gap. A blade duct length of $L = 60\text{mm}$ is chosen. Equation 3.12 gives values of $(r_c)_{exit} = 62.6\text{mm}$ and $(r_h)_{exit} = 17.4\text{mm}$. Table 2 shows the values of the remaining geometric variables. Figure 13 shows the embodiment of this design. The propulsor is modular allowing for quick part replacement and is comprised of 5 aerodynamic components and 1 electric motor (including rotor mount and spinner). The assembled propulsor has a length of 167mm and a maximum diameter (at the intake) of 180mm . Design considerations for each component are discussed below.

4.3.2 Shrouded Rotor

The rotor has 11 blades and is shrouded as in Fig. 14. The shrouding provides support for 3D printing to enable large overhangs without the blades deforming. The amount of support material required is minimised as it can adversely affect surface finish of the blades. Reflective aluminium tape is mounted to the outside of the shroud and coupled with an

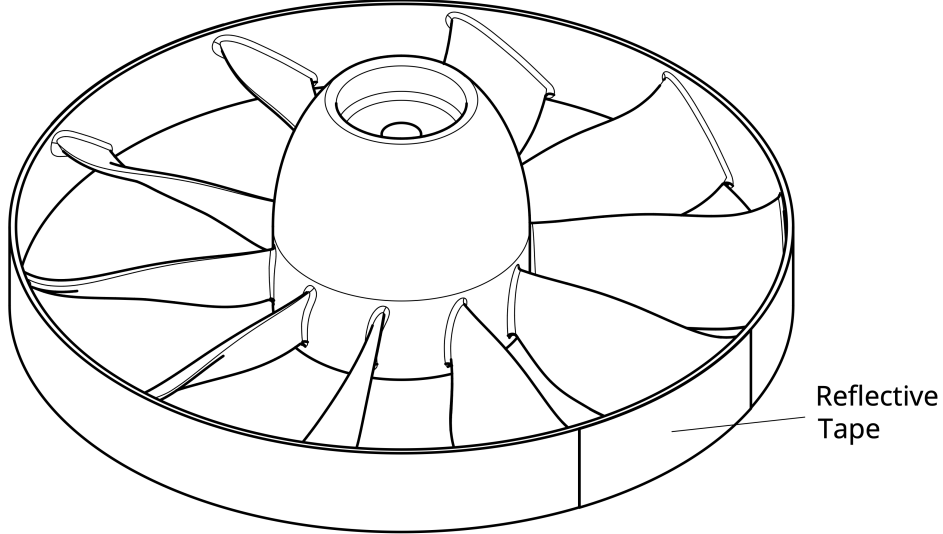


Figure 14: Isometric view of shrouded rotor

IR photo-transistor mounted to the casing to enable measurement of the rotor speed. The clearances required to ensure the shroud does not rub against the casing means the tip-gap required is large, $\approx 5\%$ of span, which introduces shroud clearance flow losses. Corner separations at the blade-shroud interface are minimised by adding lean to the blade as described in Section 3.3.6. To maintain a high quality printing finish on the trailing edge of the blade, print support should be avoided and so the blade is shifted in the axial direction to minimise the distance between the trailing edge and the build plate, located on a $r-\theta$ plane on the downstream side of the rotor. Maximum stress is expected at the blade-hub interface and so a fillet of $0.75mm$ is added to limit stress concentrations.

A finite element analysis (FEA) of the rotor at operating speed is undertaken. The rotor is fixed at the motor shaft and a centrifugal force is applied with equivalent rotor speed of 6000 RPM. A force of $5.5N$ is applied to the pressure side of the blades to simulate the thrust generated by the blades. 1st Order elements are used and the local mesh size at the blade hub is set to $\approx 0.1mm$. The von Mises yield criteria can be expressed as

$$\sigma_{yld} = \sqrt{3}k_{PLA} \quad (4.6)$$

where $k_{PLA} = 33$ MPa is the shear yield strength of 3D printed PLA as found by Anderson (2017)[12]. This gives a maximum von Mises stress of $\sigma_{yld} = 57.2$ MPa. The FEA results in Fig. 15 show the maximum von Mises stress to be $\sigma_{vm} = 10.4$ MPa giving a yield margin of safety of 4.5. Radial displacement is negligible and so shroud clearance to casing is governed by tolerances required for shroud eccentricity as a result of 3D printing. The shroud has a thickness of $1mm$ and there is a $2mm$ gap between the rotating shroud and the stationary casing.

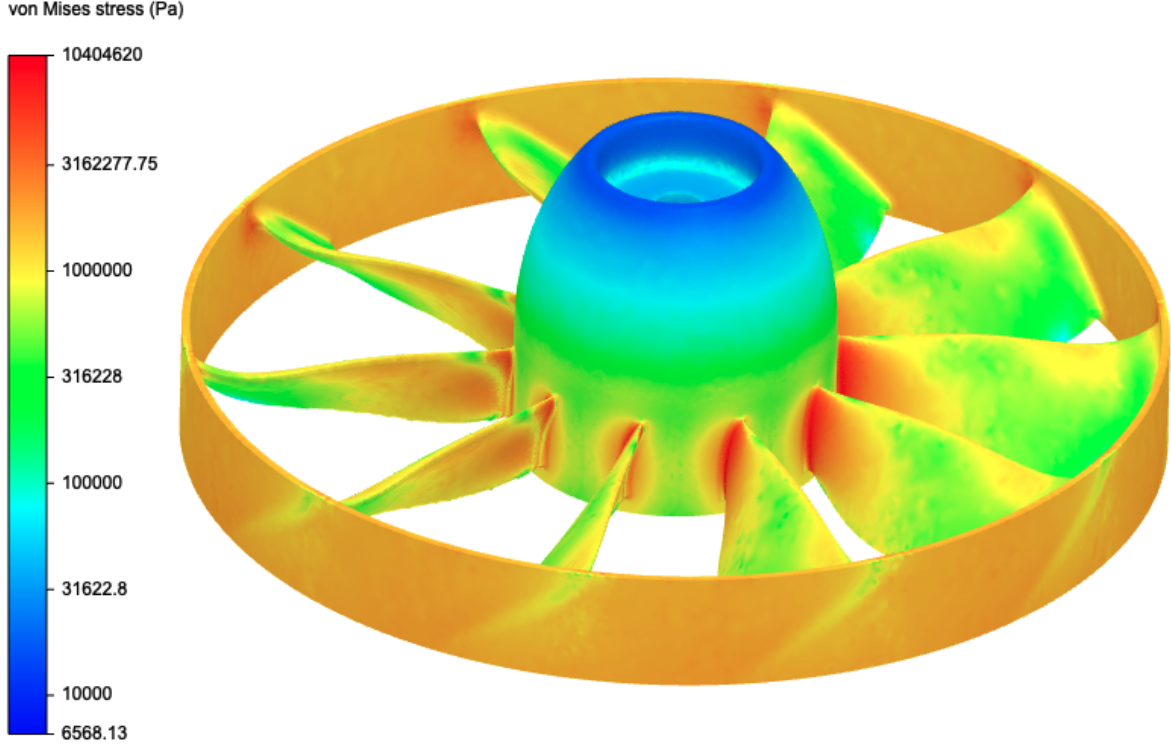


Figure 15: Finite element analysis of the rotor at operating speed with color bar showing von Mises stress with a logarithmic scale

4.3.3 Stator Block: Stator Blades, Casing, and Hub

The stator blades, casing, and hub are all one 3D printed part as shown in Fig. 16. The blades are both aerodynamic and structural components. The stators transfer the force of the fan to the drone chassis via the casing and arm. The electric motor mounts to part of the hub known as the mounting plate with 4 x M3x6 cap-head bolts. The plate has ventilation holes that match the underside of the motor to allow airflow to cool the motor and prevent overheating. Although the motor is operating at 20% rated power, maintaining airflow prevents the PLA expanding during operation which can cause warping or rubbing. The ventilation holes also allow the 3 power wires on the motor into the hub cavity below the mounting plate where they are connected to three power supply cables. These power cables are fed from the flying test bed through passages in the stator blades that can be seen as holes on the casing in Fig. 16. These passages are generated by outputting the line of maximum blade thickness and lofting a circular section along it. The 3D printer generates minimum wall thicknesses of approximately 0.3mm so to avoid the passage breaking through the stator wall the loft diameter must be less than the maximum stator thickness minus $2 \times 0.3\text{mm}$. At the hub the maximum thickness is 2.15mm therefore the maximum passage width is $2.15 - 2(0.3) = 1.55\text{mm}$. This sets the limit for power supply wire thickness. The hub provides an interference fit to the motor to reduce rotor eccentricity with respect to the

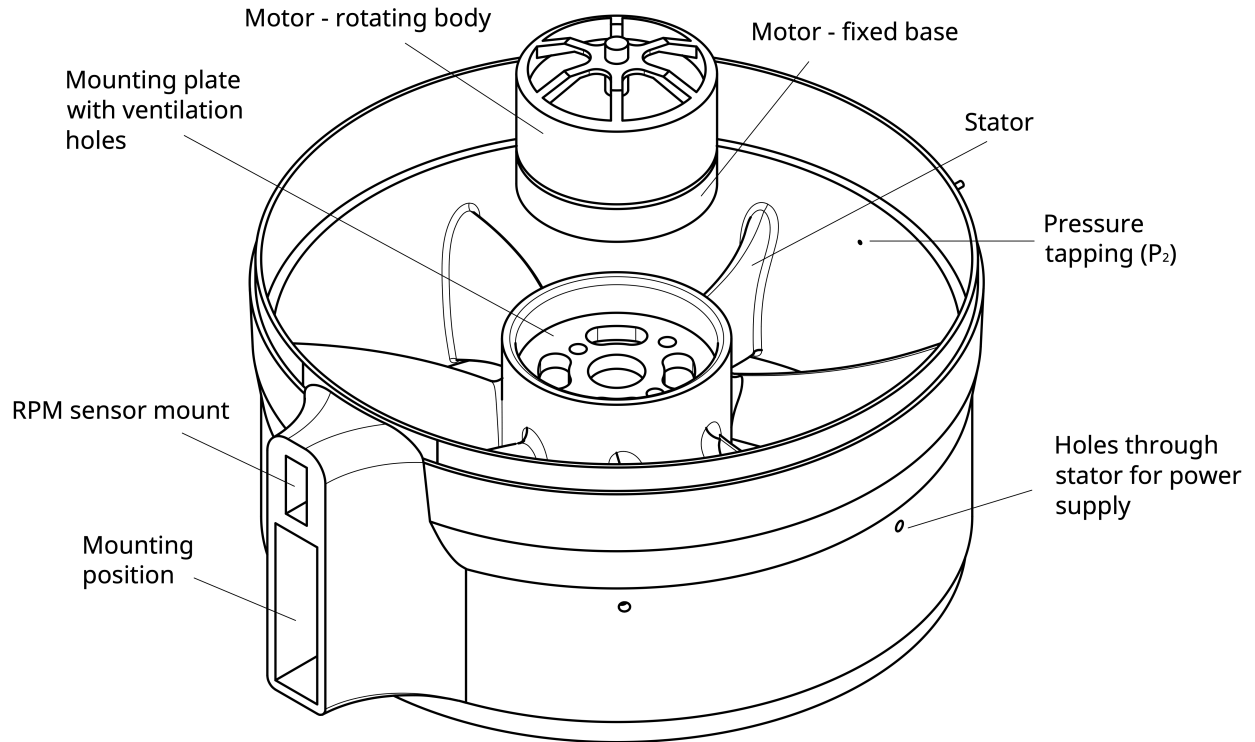


Figure 16: Exploded view of stator block and electric motor showing mounting plate with ventilation and mounting holes. Propulsor mounting point for mounting to flying test bed or stationary test rig is shown with mounting hole for IR photo-transistor

casing. The intake and diffuser sections also mount to the stator block with an interference fit. Both intake and diffuser casing are fixed in place with adhesive tape. The mounting point for the propulsor to be attached to the flying test bed or the stationary test rig is sized to the outer dimensions of the load-cell. The arm attachment is shaped like the load-cell so the same mounting point can be used.

4.3.4 Diffuser

The diffuser is mounted to the stator block via an interference fit. The casing is also held in place with adhesive tape as it is more prone to detaching under vibration than the hub. Both diffuser hub and casing are designed to be as thin as possible while remaining rigid. At exit the diffuser has a thickness of 1mm and at entry it has a thickness of 2mm.

4.3.5 Intake

The intake is mounted to the stator block via an interference fit. As it generates thrust it must be securely attached to the stator block and so adhesive tape is also used. The intake is less prone to eccentricity as it has a curved cross-section. It can be printed with a constant

thickness of $1mm$. Print times for the intake can be large as significant support material is required due to the overhang of the lip.

4.3.6 3D Printing

All structural and aerodynamic parts are made using an Ultimaker 3 3D printer and $2mm$ diameter RS Pro PLA filament. Prints are set to 75% infill with a cubic subdivision infill pattern (see Appendix B for more details on 3D printing).

5 Experimental Methods

Two types of experiment are undertaken: stationary propulsor tests and hover tests to determine system performance. All testing is done in a purpose built indoor test environment at the Whittle Laboratory. Figure 18 shows the $2.0m \times 2.2m \times 2.5m$ cage constructed with $3cm \times 3cm$ timber beam and $1cm$ grid chicken wire covering the sides to provide protection from the propulsor and flying test bed. A retrospective risk assessment analysis is conducted in Appendix C.

5.1 Cage Design & Tether

Figure 18 shows the safe indoor test environment constructed for conducting both stationary propulsor and hover tests. The $2.0m \times 2.2m \times 2.5m$ frame is constructed out of $3cm \times 3cm$ section timber beam. $5cm$ wood screws are used to fasten the beams – 2 screws are used at each intersection to add a moment constraint at each connection. An inward opening door provides access to the environment and is hung so that it closes if left open for safety. $1cm$ grid chicken wire walls are fastened securely on each beam. The wire is in tension to increase the frame's rigidity. A central beam crosses the top of the cage and acts as the mounting point for the tether. $1m$ of shock cord is attached to a long piece of parachute cord using a carabiner. The parachute cord is fed over the central beam on the top of the cage and over the cage edge above the door. It is fastened by a small screw. This allows the tether to be raised or lowered from outside of the cage.

5.2 Stationary Propulsor Test

Propulsor performance is tested on the stationary test rig, shown in Fig. 19, to determine thrust, power, RPM, and motor temperature as well as characterise the aerodynamic performance with static pressure measurements. All electronic connections are made using metallic braid shielded cable. Thrust, power, and RPM data is collected by the flying test bed chassis and the main motor outputs are used to power and control the propulsor. Temperature readings are made using an external thermometer.

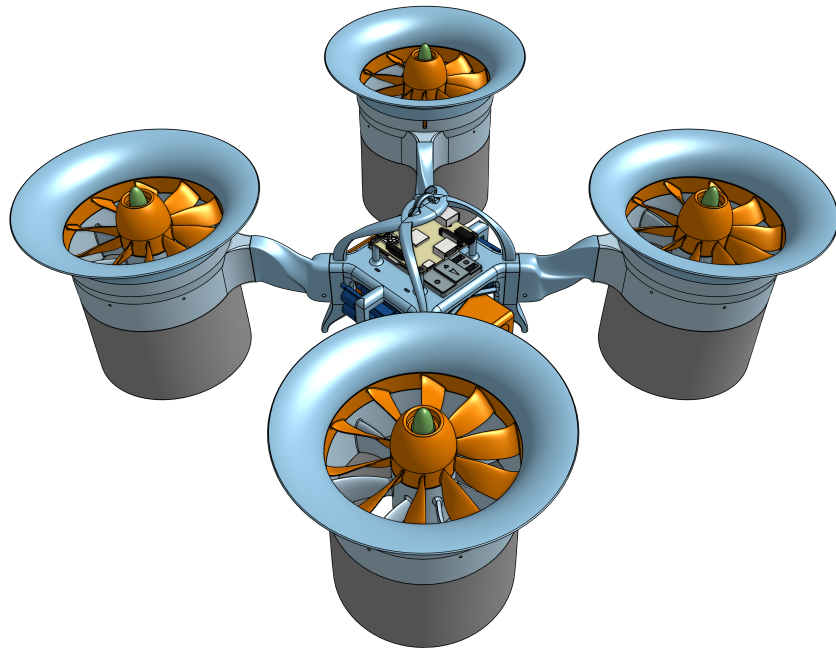


Figure 17: Perspective render of flying test bed in hover test configuration

5.2.1 Setup

Figure 19 shows the experimental setup for stationary tests in the calibration configuration. An aluminium speed-frame structure is fixed to the ground and has a horizontal mounting beam 1m in height and 1m in length. Thrust, RPM, temperature and pressure measurements require external sensors; their setup is described below. The flying test bed requirements for stationary testing is also described.

Load-cell: The propulsor is mounted at one end of the frame via a 0.6kg rated single ended shear beam load-cell mounted perpendicular to the axis of the fan. A low friction pulley is mounted to the other end of the frame with the top of the pulley in line with the axis of the fan. Light-weight high tensile fishing wire is attached to the rotor spinner and is fed over the pulley, attaching to a vertically hanging weight that is used to calibrate the load-cell. This weight can be varied in multiples of 50g up to 500g. When testing, the wire is detached from the spinner and secured so as not to interfere with the fan. The load-cell connects through an HX711 ADC/amplifier breakout board that is mounted to the frame. Data is transmitted from the HX711 to the GPIO pins of the RPi3.

IR Photo-transistor: The IR photo-transistor inserts into an interference fitted slot above the mounting point, as in Fig. 19. A potential divider circuit is connected to the output of the photo-transistor and is connected to the 5V DC/Ground and GPIO pins of the RPi3 via the shielded cable.

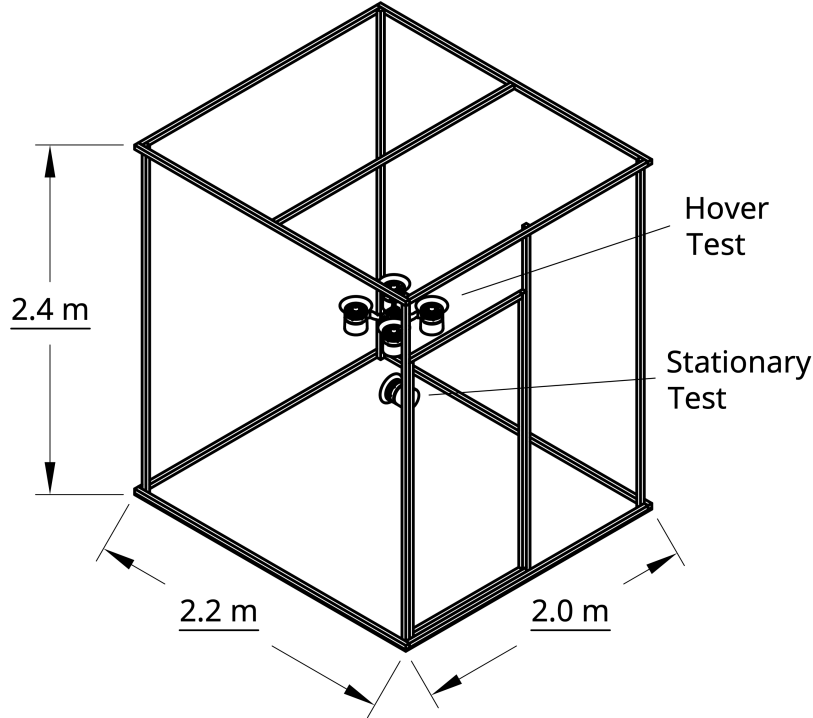


Figure 18: Test cage shown in isometric view with flying test bed in hover test configuration and an individual propulsor in the stationary test position (stationary test mount not shown)

Thermocouple: The K-type thermocouple is fixed with super glue to the motor mounting plate in the propulsor hub with the sensing junction resting against the base of the motor. The other end is fed through a hollow stator and is plugged into a K-type thermocouple external thermometer from which temperature readings are taken.

Pressure Transducers: 1.1mm holes are drilled radially into the casing at 4 axial locations as in Fig. 19: p_1 upstream of the rotor; p_2 upstream of the stator; p_3 downstream of the stator; p_e exit from exit duct. 1.1mm outer diameter hypodermic tube tappings are inserted into the holes and secured with super glue on the outside of the casing, ensuring the tapping does not protrude into the flow on the duct side of the casing. Plastic tubing with 1mm inner diameter is fixed to the end of the tappings and connected to input ports of a 16-channel external pressure transducer DSA. The DSA is connected via an Ethernet switch to the control station from which gauge pressures (relative to ambient) can be read. The DSA is positioned over 1m away from the propulsor in the $r\text{-}\theta$ plane to reduce the impact of the propulsor on the measured ambient pressure.

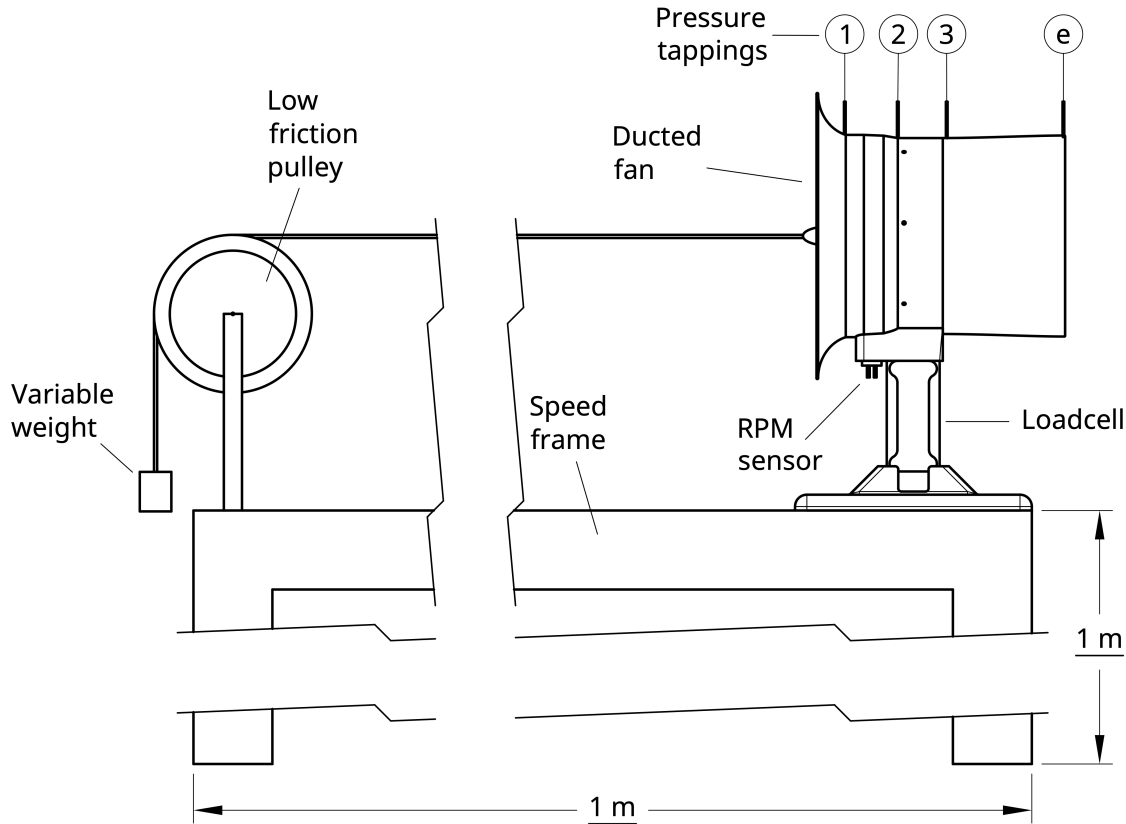


Figure 19: Experimental setup of stationary tests in calibration configuration

5.3 Hover Test

Hover tests are undertaken in the test environment by mounting propulsors to the flying test bed and conducting a static hover from a top-down tether. The hover test determines the figure of merit in flight by calculating the power required and equating vehicle weight to thrust. Vehicle stability in hover is also considered qualitatively. The propeller results allow the performance in flight to be compared to stationary tests. Further methods of testing are discussed in Section 7 on Future Work.

5.3.1 Setup

The tether ensures the flying test bed is clear of the ground to reduce any ground effect. The tether is made of 1m of shock cord (slack) to reduce stress on the structure in the event of a sudden loss in power or emergency situation in which the propulsors must be shutdown. To attach the tether to the flying test bed and act as a roll cage in the event of a collision with the topside of the chassis, an arched frame can be mounted to the chassis as in Fig. 20.

Power: In flight power usage is determined in the same way as the stationary testing.

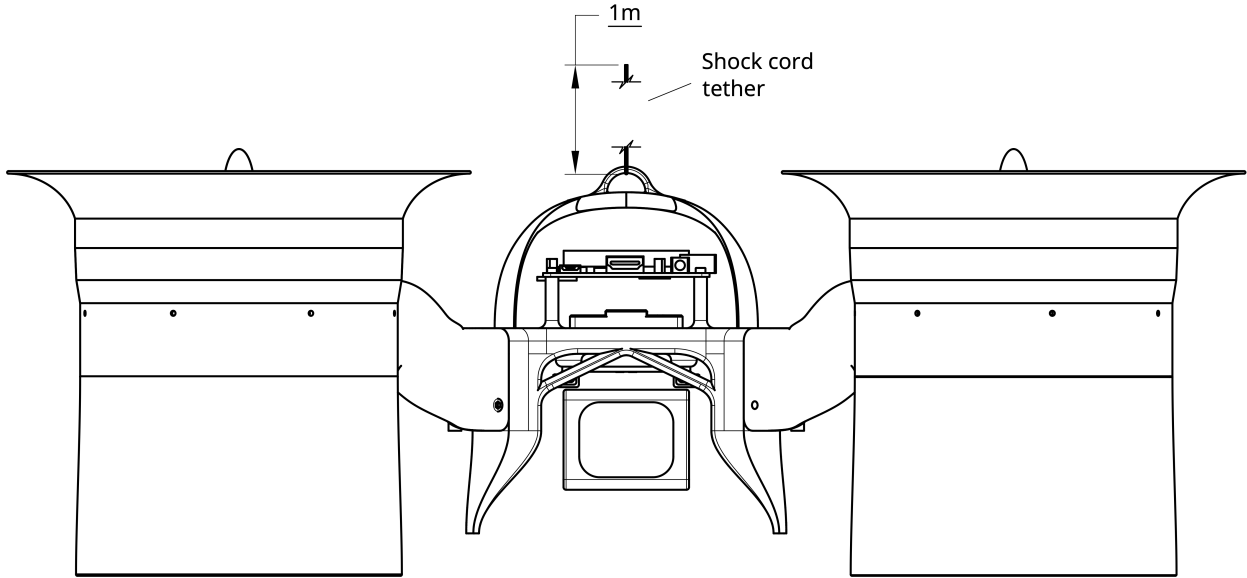


Figure 20: Front view of flying test bed in hover configuration

5.3.2 Control

The Pixhawk 4 flight controller altitude hold mode attempts to maintain the current altitude and position using its onboard GPS, accelerometers, and gyros. The indoor test environment reduces the GPS accuracy and so manual corrections are made using a handheld radio transmitter. Automatic position holding is possible using the forward-right-down ultrasound sensor array.

5.4 Measurement Techniques

Numerous measurements are made to quantify the performance of the propulsor. These measure: the overall performance in terms of the figure of merit, power required and thrust; aerodynamic performance in terms of pressure coefficients, flow coefficient and stage loading; noise levels produced by various propulsors. All measurements are taken after 5 minutes of continuous operation to reduce transient temperature effects in the motor and electronics.

5.4.1 Non-dimensional Quantities

Figure of Merit: Figure of merit is found using measured or equivalent thrust and electrical power requirement. Thrust is measured directly using the load-cell in the stationary tests but in the hover tests the thrust is taken as being equal to the flying test bed mass, which is measured prior to flight using a high precision scale. Both load-cell and scales have an accuracy of $\pm 0.1g \approx \pm 0.1\text{mN}$. Power is measured as electrical power output from the Pixhawk 4. Readings are accurate but due to noise, particularly during hover tests, they can be imprecise. Taking a mean value over a large window reduces the effect of noise. The flow

area is assumed as designed ($A_x = \pi(r_c^2 - r_h^2)$) and air density is calculated from ambient temperature and pressure.

Flow Coefficient: Flow is assumed axial at inlet and stagnation pressure equal to atmospheric pressure. Using Bernoulli's equation the axial flow velocity at the casing is determined and the flow coefficient evaluated by dividing by the local blade speed, as in Eqn. 5.2. Taking the span-wise distribution of flow coefficient to be equal to that determined in Section ?? the mean-line flow coefficient can be determined from Eqn. 3.26a

$$\phi = \phi_m \left(\frac{r}{r_m} \right)^A \implies \phi_m = \phi_c \left(\frac{r_c}{r_m} \right)^{-A} \quad (5.1)$$

$$\therefore \phi_m \approx \left(\frac{V_x}{U} \right)_c \cdot \left(\frac{r_c}{r_m} \right)^{-A} \implies \phi_m \approx \sqrt{\frac{(p_a - p_1)_c}{\frac{1}{2}\rho(\Omega r_c)^2}} \cdot \left(\frac{r_c}{r_m} \right)^{-A} \quad (5.2)$$

Static pressure p_1 is measured as gauge pressure relative to atmospheric, $p_1 - p_a$. Rotor RPM is measured using the IR photo-transistor. Casing and mean-line radius are taken as their design values.

Stage Loading: Stage loading can be estimated by assuming the exit flow from the stator is axial as well as $\partial V_x / \partial x = 0$ due to incompressibility and negligible radial velocity. Using Bernoulli the static pressure at stator exit, p_3 , can be related to the change in stagnation pressure as follows

$$\Delta p_0 = p_{03} - p_{01} \implies (p_3 + \frac{1}{2}\rho V_x^2) - p_{01} \xrightarrow{p_a} \quad (5.3)$$

Substituting Eqn. 5.3 into Eqn. 3.3, stage loading can be expressed as

$$\psi = \frac{p_3 - p_a}{\rho U^2} + \frac{1}{2} \left(\frac{V_x}{U} \right)^2 \quad (5.4)$$

where $p_3 - p_a$ is the measured gauge static pressure. A similar expression to Eqn. 5.2 can be found for stage loading and so the mean-line stage loading can be estimated by

$$\therefore \psi_c = \frac{(p_3 - p_a)_c}{\rho(\Omega r_c)^2} + \frac{1}{2}\phi_c^2 \implies \psi_m \approx \left[\frac{(p_3 - p_a)_c}{\rho(\Omega r_c)^2} + \frac{1}{2}\phi_c^2 \right] \cdot \left(\frac{r_c}{r_m} \right)^{-B} \quad (5.5)$$

Diffuser Static Pressure Recovery: Equation 3.9 shows the theoretical static pressure recovery coefficient can be expressed in terms of the exit duct area ratio, σ . Assuming V_x remains constant this is written in terms of the measured static pressures

$$C_{pr} = \frac{p_e - p_3}{\frac{1}{2}\rho V_x^2} = \frac{p_e - p_3}{p_a - p_1} \quad (5.6)$$

Thrust Coefficient: Thrust output is non-dimensionalised by mean-line blade speed and flow area, as in Eqn. 5.7

$$C_T = \frac{T}{\frac{1}{2}\rho(\Omega r_m)^2 \cdot A_x} \quad (5.7)$$

Mean-line blade speed is calculated from the recorded RPM and the design mean-line radius.

5.4.2 Data Acquisition and Processing

In this section, methods for recording and processing the data streams of thrust, power, RPM, pressure, and temperature are described. Data is collected for ≈ 30 seconds and mean values are obtained for each data stream. Mean values are used in the analysis but time-sampled data is verified to be steady.

Thrust: Prior to each test the load-cell is tared to remove any zero error. The load cell is then calibrated in order to determine the thrust developed by the propulsor. The setup described in the stationary propulsor test section allows multiple readings to be made within the load-cell's operating range. 10 different forces are applied to the propulsor using 50.0g weights and the mean of 100 readings taken at each force. The resulting data is linear in the full range of operation of the load-cell. This means a calibration must be done once as environmental variations can be accounted for by removing the zero error prior to a test. A Python script on the RPi3 manages simultaneous recording of thrust (from load-cell) and RPM (from IR photo-transistor data) and produces a `*.txt` log file that is wirelessly imported to MATLAB via the SCP protocol. Raw values are compared to the fit obtained during calibration to determine the corresponding thrust. The mean thrust is determined.

Power: Power is measured by recording the output DC voltage and current from the PM07 power management board. Maximum sample rate is $\approx 1\text{Hz}$, limited by the telemetry data transmission protocol, and so ≈ 30 readings are made. Voltage and current data is obtained through the logging feature on QGroundControl: MavLink Inspector via the telemetry module. The recorded log is automatically imported into MATLAB® for processing. Instantaneous samples of current and voltage are multiplied to determine instantaneous power. A mean power is then determined.

RPM: At operating speeds, one revolution of the rotor takes 9.63ms. Each reflective strip is 50mm in length (with negligible thickness) and is attached to the outside face of the shroud at a radius of $r_c + 1\text{mm}$ and so takes $[50/(2\pi(r_c + 1\text{mm}))] \times 9.63\text{ms} = 1.26\text{ms}$ for the tape to pass the IR photo-transistor. Therefore the minimum sample rate for the IR photo-transistor to register the tape is $1/1.26\text{ms} \approx 800\text{ Hz}$. In order to make the reading more reliable and ignore spurious reflections it is determined that 10 consecutive readings are required. This increases the minimum sample rate to 8 kHz. Allowing for 200% operating motor speed during stationary propulsor tests increases this requirement to 16 kHz. The RPi3 was found

to have a GPIO sample rate of 30 kHz therefore recording RPM from 2 propulsors would require a sample rate above this. Assuming negligible variation in electric motor and propulsor performance, all 4 propulsors should operate at a similar RPM during static hover and so one RPM reading is sufficient to determine mean rotor speed. A Python script on the RPi3 manages simultaneous recording of thrust (from load-cell) and RPM (from IR phototransistor data) and produces a *.txt log file that is wirelessly imported to MATLAB via the SCP protocol. RPM is determined by timing how long it takes for the reflective tape to be registered (10 high readings). Once 10 high readings have been made the first high is used to time the gap between reflective tape. As there are two reflective strips the frequency is halved and the average taken over 10 revolutions. This reduces the error due to the first high not being in the same place every time.

Pressure: Pressure tappings measure static pressure at the casing. Flow quantities such as flow coefficient are determined at the casing and their mean-line values are estimated from the design span-wise distributions. Pressure is measured from the DSA as gauge pressure relative to atmospheric, $p - p_a$, taking ≈ 100 readings over 30 seconds. Each reading is made up of 1000 instantaneous samples. Measurements are made simultaneously with thrust, power, RPM, and temperature measurements to synchronise the data and account for any transient behaviour. Data is recorded directly into MATLAB on the control station. Non-dimensional quantities are calculated as in Section 5.4.1. The mean is calculated over the 100 readings.

Temperature: One K-type thermocouple is fixed to the mounting plate of the electric motor in the ducted fan hub. This is connected via a 1m long cable to a thermocouple thermometer that is mounted on the vertical portion of the stationary test rig frame. Whilst data is collected the temperature is monitored to ensure it remains below 50°C, well below the PLA glass transition temperature of 60 – 65°C. Temperature readings are made during the stationary tests but cannot be made during hover tests.

6 Results

6.1 Stationary Propulsor Test

Three significant sets of ducted fan testing were completed (see Appendix A). The performance of two different lengths of intake are compared. Free vortex and mixed vortex design rotors are also compared. Finally diffuser performance is analysed at the design point. The design parameters used in each design are outlined as they vary from the final design described in Section 3. First, the electrical efficiency of the flying test bed and motor must be determined to account for these losses when considering other propulsors.

6.1.1 System and Electrical Efficiency

System electrical efficiency can be estimated by comparing experimental data for the APC propeller to the manufacturers calibration data. The shaft figure of merit, defined using the power at the shaft, $P_s = \Omega \cdot T_s$, can be determined from the calibration data. Assuming any aerodynamic losses are incurred equally by both experiment and calibration data, the difference in figure of merit can be accounted for by the electrical efficiency of the motors and flying test bed. The thrust produced at a given RPM is therefore equal and so difference in figure of merit is due to power. Therefore the electrical and system efficiency, $\eta_{sys.}$, can be found by the ratio of the experimental to the calibration data figure of merit.

$$\eta_{sys.} = \frac{(M_F)_{exp.}}{(M_F)_{cal.}} \quad (6.1)$$

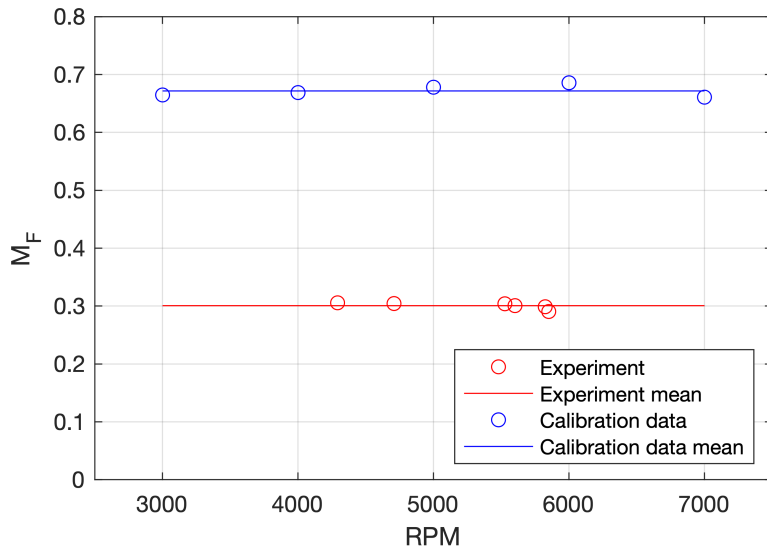


Figure 21: Figure of merit for APC propeller from experiment and calibration data

Figure 21 shows the figure of merit determined for the APC propeller from both experiment and calibration data to vary only a small amount with RPM in the range of interest and so the system efficiency is assumed constant. The electrical and system efficiency is calculated using the mean values from each dataset and is found to be

$$\eta_{sys.} = \frac{0.301}{0.672} = 45\% \quad (6.2)$$

This can be used to estimate the shaft figure of merit of any propulsor tested on the stationary test rig. The shaft figure of merit of the APC propeller is

$$(M_{F,s})_{APC} = 0.67 \quad (6.3)$$

6.1.2 Ducted Fan Figure of Merit (*Version 3.1*)

Three preliminary ducted fans were tested. 2D design is the same as described in Section 3.2 but 3D design variations from Section 3.3 are outlined in Table 6, alongside the recorded figure of merit and the shaft figure of merit. Version 3.1 used a higher quality 3D printer configuration than Version 2.2 but they are otherwise identical. Shaft figure of merit is calculated using the system efficiency calculated above. Ducted fans are shown to have a higher figure of merit than both the propellers in experiment and the theoretical maximum figure of merit for a propeller, $M_{F,max} = 1$. Aerodynamic efficiency is defined in terms of shaft figure of merit as

$$\eta_a = \frac{M_{F,s}}{M_{F,max}} \quad (6.4)$$

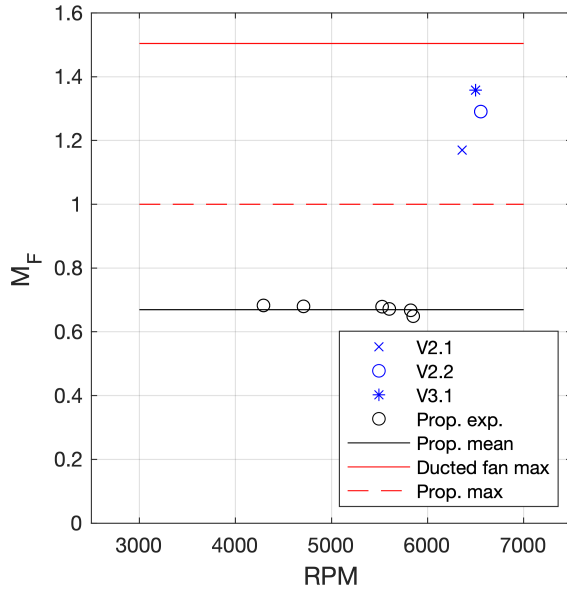
Version	-B	DF	N	$M_{F,exp.}$	$M_{F,s} = M_{F,exp.}/\eta_{sys.}$
(Final Design	1.7	0.25 → 0.4	11	-	Pred. = 1.51)
2.1	1.2	0.45	7	0.524	1.17
2.2	2.0	0.45	7	0.578	1.29
3.1	2.0	0.45	7	0.608	1.36

Table 6: Test design parameters and figure of merit

where $M_{F,max}$ represents the theoretical maximum figure of merit given for a propeller as $M_{F,max} = 1$ and for a ducted fan with exit duct area ratio σ as $M_{F,max} = \sqrt{2\sigma}$. Table 22b shows the calculated aerodynamic efficiencies of the fans. All ducted fans have a mean-line operating point of $\phi_m = 0.8$ and $\psi_m = 0.25$ and therefore $M_{F,max} = 1.51$. The sources of aerodynamic loss are hypothesised to come from 3 main sources. The first is tip loss due to shroud clearance flows. The second is flow separation from the blade due to low Reynolds number effects. Finally manufacturing techniques introduce geometric uncertainty as well as high surface roughness that can affect the flow.

Shroud Clearance Flows: Denton (1993)[13] describes a loss model due to mixing in shroud clearance flows. All flow angles are taken in the blade relative frame at the casing.

$$\frac{T\Delta s}{\frac{1}{2}V_2^2} = 2 \frac{m_l}{m_m} \left(1 - \frac{\tan \beta_1}{\tan \beta_2} \cdot \sin^2 \beta_2\right) \quad (6.5)$$



(a) Figure of merit for ducted fans compared to the propeller data

Version	η_a
2.1	0.78
2.2	0.86
3.1	0.90

(b) Aerodynamic efficiencies of ducted fan designs

Figure 22: Performance and efficiency of Versions 2.1, 2.2, and 3.1 ducted fans

where the fractional leakage is given in terms of tip clearance, g , blade span, h , and rotor relative flow angles

$$\frac{m_l}{m_m} = \frac{g}{h} \sqrt{\sec^2 \beta_2 - \tan^2 \beta_1} \quad (6.6)$$

For the design described in Section 3.3 this gives a loss coefficient of

$$\frac{T\Delta s}{\frac{1}{2}V_2^2} = 0.0093 \approx 1\% \quad (6.7)$$

This is a result of the a large shroud clearance of $\approx 2mm = 5\%$ of span. This clearance is required due to manufacturing tolerances.

Low Reynolds Separation: Using the casing pressure tappings at inlet to the fan the casing flow coefficient and axial velocity can be estimated. This allows the variation in Reynolds number across the span to be estimated by assuming the flow coefficient distribution across the span is as designed any any variation is due to a constant offset in axial velocity. Experiment shows the casing flow coefficient to be $\phi_{c,exp.} = 0.551$ compared to the design value of $\phi_c = 0.593$. The result is Reynolds number variation shown in Fig. 24. Though care is taken to reduce surface roughness, the manufacturing process necessitates span-wise ridges on the surface of the blade as 3D printed layer thickness is finite, $\approx 0.1mm$ in this design which is at the order of 1% of chord. Figure 24 shows the Reynolds number to

be the lowest at less than 20,000 at the hub where the diffusion factor is also highest implying strongest adverse pressure gradients. It is therefore hypothesised that the combination of high surface roughness, low Reynolds number flow, and an adverse pressure gradient will likely cause non-reattaching turbulent separation on the blade, resulting in loss. This loss is likely concentrated at the hub where diffusion factor and flow turning is highest. This roughness could be reduced by printing the blades in a radial direction so that the ridges resulting from printing layers are in the direction of the flow only. For this to be possible a printer that uses a cylindrical coordinate system must be developed.

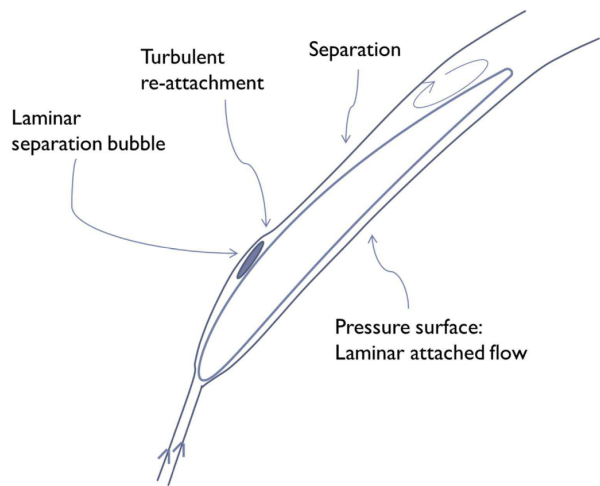


Figure 23: Typical boundary layer behaviour for low Reynolds number blade profiles in $\approx Re = 5 \times 10^4$ reproduced from Maffioli et al. (2015)[4]

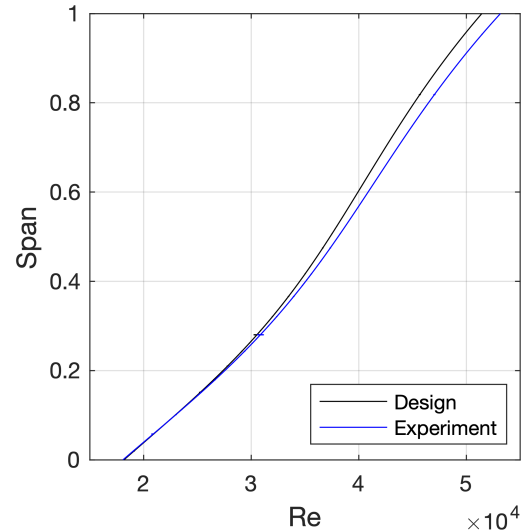


Figure 24: Estimated Reynolds number profile from experimental casing data and design spanwise distribution

Manufacturing Process: 3D printing the rotor blades introduces geometric deviations from the design in the form of surface roughness, large required clearances (both already discussed) but also warping and shrinkage. The FEA conducted in the design section shows the rotor geometry to have negligible deflection under load however as high temperature gradients are required to extrude filament in order to 3D print, temperature gradients can be expected throughout the structure. These gradients impart thermal strain on the structure that can cause warping after cooling. The geometry of the printed part can be analysed using a 3D scanner and any geometric deviation quantified. Potential solutions to this problem include higher fidelity printing, ambient temperature regulation when printing, controlled cooling after printing, and annealing.

6.1.3 Ducted Fan Mass Model – ΔW

Figure 25 shows the mass model predicted mass compared to the manufactured ducted fan mass. The model predicts the propulsor mass with an accuracy of 8%, suggesting the mass model is valid at the scale considered here. It should be noted that mechanical and structural considerations at larger fan diameters and higher thrusts may cause the model to deviate further from the manufactured propulsor. The choice of material and manufacturing method may change with size and application at which point the model may need updating, though the same modelling principles should still be valid.

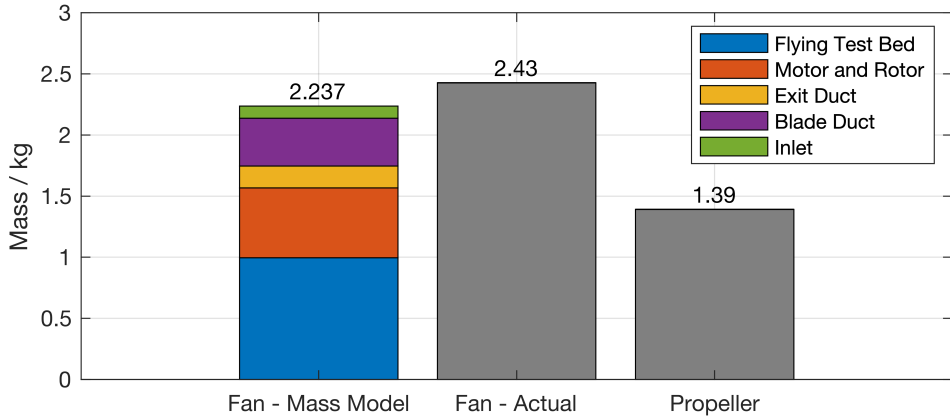


Figure 25: Comparison of flying test bed mass when driven by propellers or ducted fans. Mass model is compared to measured mass of vehicle for the ducted fan design

Considering the ducted fan performance criteria presented in Eqn. 1.13, the LHS of this inequality can now be determined.

$$\frac{W_{fan,total}}{W_{prop.,total}} = \frac{2.43}{1.39} = 1.75 \quad (6.8)$$

Showing that the ducted fan propulsors mounted to the flying test bed account for approximately 40% of the vehicle weight. This could be reduced through the use of advanced materials such as carbon composites to form a lightweight yet stiff casing structure.

6.1.4 Superiority Condition

Taking the superiority condition for a non-ideal propeller, from Eqn. 1.12 we obtain

$$\frac{W_{fan,total}}{W_{prop.,total}} \leq \left[\frac{(M_{F,s})_{fan}^2 A_{x,fan}}{(M_{F,s})_{prop.}^2 A_{x,prop.}} \right]^{\frac{1}{3}} \quad (6.9)$$

From experiment, Eqn. 6.8 and Eqn. 6.3

$$\frac{W_{fan,total}}{W_{prop.,total}} = 1.75 \quad (\text{a}) \quad \left[\frac{(M_{F,s})_{fan}^2 A_{x,fan}}{(M_{F,s})_{prop.}^2 A_{x,prop.}} \right]^{\frac{1}{3}} = 0.933 \quad (\text{b}) \quad (6.10)$$

The superiority condition is not satisfied. This result was predicted in the design section and is a result of the propulsor weight being too large with respect to the payload weight. Section 7 discusses this idea further. Figure 28a (see Section 7 shows the same design conditions as in Fig. 7b but with a payload of 15kg and the recorded values of figure of merit for the ducted fan and propeller. This shows there to be a point in the design space that maximises the superiority condition, provided a large fan is used and a large enough payload is carried. This method assumes the correct blade operating point (ϕ, ψ) is selected meaning the approximate Reynolds operating point must first be determined.

6.1.5 Intake Performance (*Version 1.0 EDF*)

The two intake designs compared are shown in Table 27. The short intake produces audibly unsteady flow as the tone generated by the fan changes with a corresponding $0.5 - 2\text{Hz}$ variation cycle. It is hypothesised that this is due to flow separation at the intake causing either part or full circumference tip stall. No significant cyclic variation in tone is observed with the long intake. The figure of merit of the long intake was found to be 30% higher than the short intake thus supporting these observations. The long intake was used in all other tests described here.

6.1.6 Diffuser Performance (*Version 2.0 EDF*)

Diffuser performance is assessed assuming exit flow is straight and parallel. The coefficient of static pressure recovery across the diffusers of Version 2.1 and 2.2 fans is presented in Table 26. This shows the static-pressure recovery to be considerably lower than designed. Both the Version 2.1 and 2.2 ducted fans had a pressure tapping upstream (P_3) and downstream ($P_{diff,in.}$) of the joining line where the diffuser casing meets the stator block at the same design radius. Version 2.x manufacturing issues resulted in the trailing edge of the stator block being rough and slightly eccentric. The static pressure difference should be negligible between $P_{diff,in.}$ and P_3 however it is found that for both 2.1 and 2.2 the static pressure loss (normalised by flow velocity) is $P_{diff,in.} - P_3 / 0.5\rho V^2 \approx 0.1$. This suggests the flow separated at the joining line resulting in a loss in diffuser performance. The manufacturing issues experienced with the Version 2.x fans were resolved for Version 3.x.

6.1.7 Vortex Design (*Version 2.0 EDF*)

Version 2.1 and 2.2 ducted fans compare the performance of a low mixed vortex design ($-B = 1.2$) and a free vortex design ($-B = 2$). The two fans differ only in the rotor used. Table 22b shows the significant difference in efficiency between the two designs, and resulting difference in figure of merit. Table 26 shows the coefficient of thrust for each propulsor.

Version	Design C_{pr}	Exp. C_{pr}	C_T
2.1	0.22	0.0733	0.0535
2.2	0.22	0.0786	0.0491

Figure 26: Coefficient of diffuser static pressure recovery and coefficient of thrust for Versions 2.1 and 2.2 ducted fan

	Intake	Length	Radius
Short	$0.3 \times r_c$	$1.1 \times r_c$	
Long	$0.7 \times r_c$	$1.5 \times r_c$	

Figure 27: Approximate intake dimensions

Version 2.1 has a higher coefficient of thrust though it has a lower blade speed, coming at the cost of efficiency. Producing more thrust at a lower speed is useful for applications where tip speed is limited, or applications that require lower noise output (resulting from lower speed) and do not have strict efficiency requirements.

6.2 Hover Tests

Hover tests are conducted for APC VTOL optimised propellers to verify the method. Preliminary results are presented here and compared to those obtained in stationary tests.

6.2.1 Propeller Performance

The figure of merit recorded was ≈ 0.3 . This suggests that in-flight performance is comparable to stationary test performance.

6.2.2 Hover Test Limitations

The error observed in the flight data was large due to variations in thrust resulting from the control system attempting to maintain position. This resulted in frequent spikes in the power. Combining this error with the low sampling rate for power readings made it difficult to determine the exact figure of merit. As the propellers were unshrouded extreme care was taken to avoid contact with the test cage walls which likely resulted in more manual position corrections than necessary. This will improve when testing ducted fans as the casing will provide shielding against contact. As a result of the test environment being small and in close proximity to solid walls, there was significant wall effect further adding to the difficulty to maintain horizontal position. A larger test environment or testing outside on a calm day could be suitable alternatives. More emphasis should be placed on tuning the control system once the ducted fans have been mounted to ensure smooth motion and reduce the magnitude of power spikes.

7 Future Work

This report has acknowledged the vastness of the design space and established the validity of pursuing alternative methods of propulsion to the propeller. Further work must be carried out to better understand the design space, consider other propulsor configurations, and explore the response of a ducted propulsor in a dynamic environment. These themes are discussed in this section.

7.1 Propulsor Design

7.1.1 Exploration of the Superiority Condition

The superiority condition adds a design constraint that enables comparative performance to be determined. Taking Eqn. 1.13 and substituting the propulsor thrust in Eqn. 3.7 for its weight gives

$$\frac{W_P}{(A_{x,prop.})^{\frac{1}{3}}} \geq \rho \pi^{\frac{2}{3}} \Omega^2 \frac{\phi_m^2}{(2\sigma)^{\frac{4}{3}}} \frac{r_c^4 - r_h^4}{(r_c^2 - r_h^2)^{\frac{1}{3}}} \quad (7.1)$$

Equation 7.1 shows the relationship between the ducted fan design parameters and the geometry of an ideal propeller. Expressing the condition in this way allows the design space to be explored further. This suggests an increase in payload will allow the superiority condition to be satisfied – Fig. 28a demonstrates this by evaluating the design at with a much larger payload and finding a local maximum to the superiority condition in terms of geometric variables. Alternatively thrust density of the propulsor could be increased to reduce the number of propulsors required for hover. This is explored further in Section 7.1.2.

7.1.2 Contra-rotating Ducted Fan (CRDF)

CRDFs replace the stator in a normal ducted fan with another rotor spinning in the opposite direction. This means the work done on the flow can double. This increase in work can be ‘cashed-in’ in a number of ways. Assuming each rotor has a flow coefficient and stage loading ϕ_1, ϕ_2 and ψ_1, ψ_2 respectively, and considering velocity triangles with rotor 1 relative angles β and rotor 2 relative angles γ , and that axial velocity is conserved along the duct

$$\frac{\psi_1 U_1}{\tan \beta_2 - \tan \beta_1} = \frac{\psi_2 U_2}{\tan \gamma_2 - \tan \gamma_3} \quad (7.2)$$

It can further be shown that

$$\tan \alpha_1 + (\tan \beta_2 - \tan \beta_1) = (\tan \gamma_2 - \tan \gamma_3) + \tan \alpha_3 \quad (7.3)$$

Hence assuming axial flow at inlet ($\alpha_1 = 0$) and exit ($\alpha_3 = 0$), Eqn. 7.2 becomes simply

$$\psi_1 U_1 = \psi_2 U_2 \quad (7.4)$$

Therefore assuming both rotors are loaded equally during steady operation this suggests they must also have equal rotor speeds. This result is also shown by Waldren et al. (2019)[14]. However Waldren shows that the overall performance of a contra-rotating stage can be described by considering the pair of rotors in the reference frame of the downstream rotor, such that the machine looks like a conventionally rotating machine with rotor speed $|U_1|+|U_2|$ in a frame of reference rotating at U_2 . As a result the relative frame CRDF non-dimensionals, ϕ' and ψ' , can be related to the absolute frame non-dimensionals by

$$\psi' = \frac{\phi'^2}{4\sigma^2} \implies \frac{\psi'}{\phi'^2} = 2 \cdot \frac{\psi}{\phi^2} \quad (7.5)$$

As efficiency is governed by the relative frame non-dimensional, this implies that using a CRDF would enable more of the design space to become accessible resulting in higher absolute frame flow coefficients without compromising efficiency. For example keeping $\psi' = \psi$ implies a higher absolute frame flow coefficient can be achieved whilst keeping the relative frame flow coefficient the same as the normal ducted fan design. From Eqn. 3.7 a higher flow coefficient will result in an increase in thrust meaning fewer propulsors are required and so the LHS of the inequality ($W_{fan,total}/W_{prop,total}$) decreases (this idea is similar to increasing the payload as in Fig. 28a which shows the superiority condition at the same design point with a 15kg payload). As the relative ducted fan performance is governed only by the figure of merit – a function of exit duct area ratio alone – and flow area – unchanged no matter how many fans are in the passage – the RHS of the inequality will remain unchanged².

Yaw Control: If a VTOL vehicle has fixed propulsors, yaw control is obtained by varying the rotor speed to impart a reaction moment on the vehicle. A CRDF with matched rotor speeds however cannot impart a moment on the vehicle as any moment generated by one rotor changing speed is cancelled out by an equal and opposite moment generated by the other rotor. Moment reaction control would require the two rotors to have unmatched speeds. Assume speed of rotor 2 is fixed and rotor 1 speed can vary to induce a moment on the vehicle. Combining Eqn. 7.3 and Eqn. 7.2, Eqn. 7.4 can be rewritten in the general form

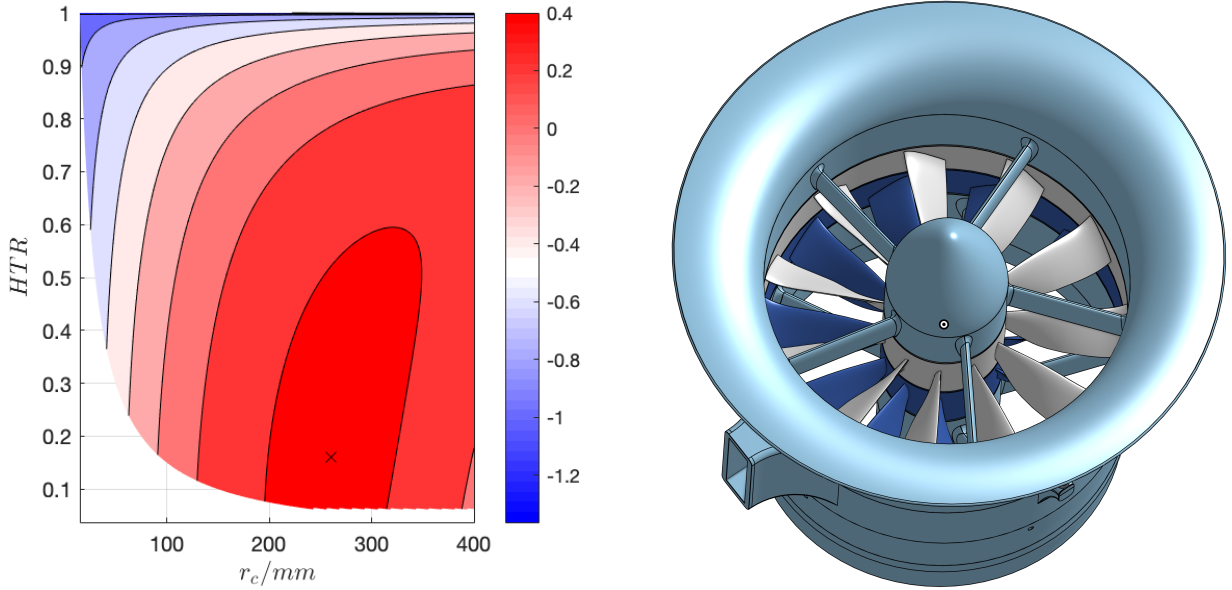
$$1 + \frac{\tan \alpha_3 - \tan \alpha_1}{\tan \gamma_2 - \tan \gamma_3} = \frac{\psi_1 U_1}{\psi_2 U_2} \quad (7.6)$$

This means variable guide vanes are required to allow moment reaction yaw control without operating off design. A simpler solution is to actuate the propulsors enabling yaw control by thrust vectoring.

7.1.3 Computational Fluid Dynamics (CFD)

Empirically obtained results such as Carter's rule and Lieblein's diffusion factor are obtained from experiments on compressor cascades, assumed to approximate an infinite radius

²Evidence suggests small increases in efficiency may be achieved by using a CRDF[14] and so the actual figure of merit may begin to approach the theoretical maximum.



(a) r_c -HTR design space showing the superiority condition given a payload of 15kg. Marked position indicates local maximum (RHS - LHS = 0.45; $r_c = 260\text{mm}$; $HTR = 0.161$)

(b) Render of CRDF design candidate

Figure 28: Proposed future work

compressor with a finite span. This assumes secondary flow effects are minimal. However for a low HTR design at a finite and small radius, the validity of these correlations is unknown. Loss mechanisms and flow behaviour assumptions could be validated using CFD. McEveley (2020)[15] explores the use of CFD in small low Reynolds number ducted fans and demonstrates suitable corroboration with experiment.

7.2 Stationary Propulsor Experiments

The design discussed in Section 3 must now be tested. It should be manufactured using the higher quality 3D printing settings used in the Version 3.1 fan as this showed a significant improvement in diffuser performance and overall figure of merit. A fan characteristic should be obtained by running the fan with varying back pressure to change the operating point. Ideally an exit traverse would also be undertaken to determine stagnation pressures across the annulus and analyse potential sources of loss. Alternative manufacturing techniques should be considered to satisfy the superiority condition using lighter propulsors. Finally a comparable CRDF design should be tested to verify increased thrust and constant figure of merit for a lower propulsor weight

7.3 Flying Test Bed Experiments

Two developments are considered here to extend the capabilities of the flying test bed. Firstly the addition of various sensors to the flying test bed for static hover tests is discussed. Secondly using the flying test bed to analyse the stability of ducted fans whilst manoeuvring is discussed.

7.3.1 Static Hover Test Adaptations

The hover test setup provides multiple interfaces for further data collection through the RPi3. RPM, noise output, and pressures could be added to the flying test bed hover test. Potential setups for these are discussed.

RPM: A single RPM sensor could be used during hover tests. To ensure the RPi3 sample rate on the IR photo-transistor output is high enough to register both reflective strips every revolution, only one sensor can be used. For static hover testing this is sufficient as each motor should have approximately equal speeds.

Noise: Acoustic noise generated by the flying test bed can be measured by an external microphone kept at a fixed horizontal distance, 1m for example. This allows the noise output by the ducted fan and the propellers to be compared.

Optional Pressure Transducers: The ADCPi ADC breakout on the RPi3 allows pressure transducers to be connected directly to the flying test bed. Two breakout boards can be stacked to give a total of $6 + 8 = 14$ inputs pressure transducer readings (2 inputs from the first ADC are used by the horizontal proximity ultrasounds and each ADC has 8 input channels).

7.3.2 Manoeuvre Tests

One drawback of the ducted design is the presence of the intake and casing upstream of the rotor. In a crosswind, or during horizontal translation of the propulsor, the flow moves across the intake and is at risk of separating off the leading edge of the intake. This results in turbulent flow passing into the windward side of the rotor resulting in a destabilising moment on the propulsor.

This moment would be easily measured in a static wind-tunnel environment[1] but the impact this has on in-flight manoeuvrability is considered more important. Consider a horizontal manoeuvre in which the flying test bed attempts to achieve a constant horizontal velocity whilst maintaining altitude. The resulting crosswind may begin to separate off the leading lip of the intake, resulting in a decrease in propulsor thrust at the current motor speed. As the propulsor must be angled to provide both forward thrust and lift, a drop in thrust results in a decrease in lift as well as a destabilising moment as in Fig. 29. Therefore the control system would demand a higher motor RPM to ensure sufficient lift.

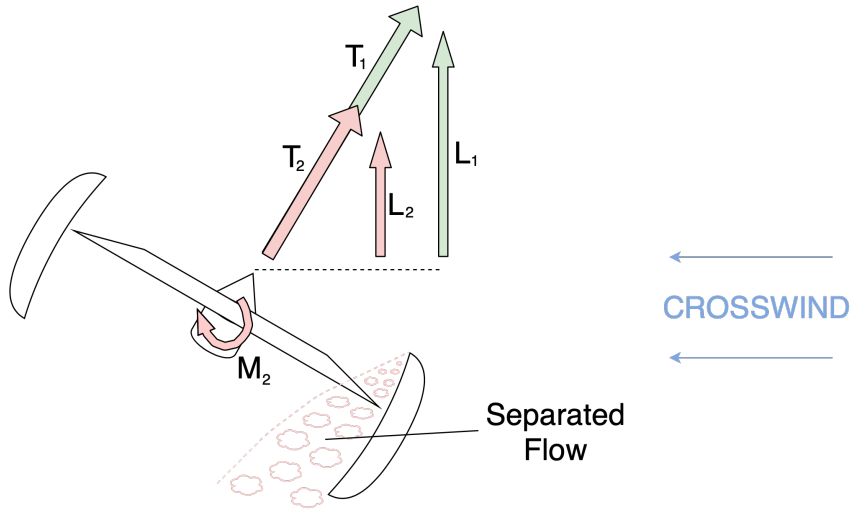


Figure 29: Effect of separation of leading lip during horizontal manoeuvre

One proposed measure of manoeuvre stability is the power requirement to maintain steady horizontal translation at a fixed altitude normalised by the power required for static hover.

8 Conclusions

Refer to questions!

1. Can an exit duct exit area ratio greater than 1 and a corresponding figure of merit greater than $\sqrt{2}$ be achieved?
2. For a specific application and design context can the superiority condition be satisfied?
3. Does performance in-flight reflect predicted performance from stationary tests?

References

- [1] J. L. Pereira, “Hover and wind-tunnel testing of shrouded rotors for improved micro air vehicle design”, MARYLAND UNIV COLLEGE PARK DEPT OF AEROSPACE ENGINEERING, Tech. Rep., 2008.
- [2] T. Zhang and G. N. Barakos, “Review on ducted fans for compound rotorcraft”, *The Aeronautical Journal*, pp. 1–34, 2019.
- [3] E. S. D. Unit, “Performance of circular annular diffusers in incompressible flow”, Engineering Sciences Data Unit, Tech. Rep., 1975.

- [4] A. Maffioli, C. Hall, and S. Melvin, “Aerodynamics of low reynolds number axial compressor sections”, in *53rd AIAA Aerospace Sciences Meeting*, 2015, p. 1934.
- [5] R. Corralejo and P. Harley, “Smith diagram for low reynolds number axial fan rotors”, in *12 th European Conference on Turbomachinery Fluid dynamics & Thermodynamics*, EUROPEAN TURBOMACHINERY SOCIETY, 2017.
- [6] S. L. Dixon and C. Hall, *Fluid mechanics and thermodynamics of turbomachinery*. Butterworth-Heinemann, 2013.
- [7] S. Lieblein, F. C. Schwenk, and R. L. Broderick, “Diffusion factor for estimating losses and limiting blade loadings in axial-flow-compressor blade elements”, NATIONAL ADVISORY COMMITTEE FOR AERONAUTICS CLEVELAND OH LEWIS FLIGHT . . . , Tech. Rep., 1953.
- [8] A. R. Howell, “Fluid dynamics of axial compressors”, *Proceedings of the Institution of Mechanical Engineers*, vol. 153, no. 1, pp. 441–452, 1945.
- [9] A. Howell, “Design of axial compressors”, *Proceedings of the Institution of Mechanical Engineers*, vol. 153, no. 1, pp. 452–462, 1945.
- [10] A. D. Carter, *The low speed performance of related aerofoils in cascades*. HM Stationery Office, 1950, vol. 29.
- [11] J. V. Taylor and R. J. Miller, “Competing Three-Dimensional Mechanisms in Compressor Flows”, *Journal of Turbomachinery*, vol. 139, no. 2, Oct. 2016, 021009, ISSN: 0889-504X. DOI: 10.1115/1.4034685. eprint: https://asmedigitalcollection.asme.org/turbomachinery/article-pdf/139/2/021009/6305774/turbo_139_02_021009.pdf. [Online]. Available: <https://doi.org/10.1115/1.4034685>.
- [12] I. Anderson, “Mechanical properties of specimens 3d printed with virgin and recycled polylactic acid”, *3D Printing and Additive Manufacturing*, vol. 4, no. 2, pp. 110–115, 2017.
- [13] J. D. Denton, “The 1993 igt scholar lecture: Loss mechanisms in turbomachines”, 1993.
- [14] J. Waldren, C. Clark, S. Grimshaw, and G. Pullan, “Non-dimensional parameters for comparing conventional and counter-rotating turbomachines”, in *Turbo Expo: Power for Land, Sea, and Air*, American Society of Mechanical Engineers, vol. 58561, 2019, V02BT40A026.
- [15] M. McEveley, “4th year project report: Propulsion systems for vtol electric vehicles”, Cambridge University Engineering Department, Tech. Rep., Jun. 2020.

Appendix A: COVID-19

The amount of testing and data collection that could be done was significant reduced due to university restrictions on residence in Cambridge and access to the Whittle Laboratory.

Fit type	Tolerance
Interference	0.15mm
Clearance (eccentricity)	1mm

Figure 30: Tolerances for various fit types with 75% infill and cubic subdivision infill pattern on an Ultimaker 3

Component	Build time
Rotor	13 hours
Stator block	1 day, 6 hours
Intake	1 day
Diffuser hub	3 hours
Diffuser casing	6 hours

Figure 31: Approximate build times for propulsor components with 75% infill and cubic subdivision infill pattern on an Ultimaker 3

I was in isolation with suspected COVID from 17th March after which Girton College was advising students to leave college. After completing isolation and following the advice of the college I relocated out of Cambridge and was unable to return. Access to the Whittle Laboratory was then restricted. Testing of the final ducted fan design (planned start 2nd April 2020) was not possible and so Version 2.1, 2.2 and 3.1 prototypes were instead used to explore the use of ducted fans. These initial versions were intended to verify and fine tune the manufacturing process as well as explore design variables, such as vortex design and intake design. Hover testing was restricted to the preliminary tests conducted after the construction of the flying test bed and so only propeller driven hover tests were conducted.

Adaptations to Final Report

The report is focused primarily on the design process and presents what data is available to back up the design philosophy. There are some differences in the design discussed and the design of the fans that were able to be tested as the design process was not complete before access to the Whittle laboratory was no longer possible.

Appendix B: 3D Printing Guidelines

All structural and aerodynamic parts are rapidly prototyped using an Ultimaker 3 3D printer and 2mm diameter RS Pro PLA filament. CAD models of parts are exported as *.stl files and sliced using Ultimaker CURA, outputting *.gcode files to be read by the printer. All parts are 3D printed in the Whittle Laboratory 3D printer room.

Tolerance: Prototyping test articles showed the printer to have the following approximate tolerances for various fit types when printing with 75% infill and cubic subdivision infill pattern.

Build-plate Adhesion: The build-plate adhesion type ‘raft’ provided suitable adhesion for printing annular bladed structures. As the trailing edges of the blades are thin (\approx 1 line width) adhesion is poor. This can be solved by using a raft and reducing the param-

eter ‘Raft Air Gap’ to ensure good adhesion between the raft and the first layer of the model.

Build Times: Table 31 outlines the approximate build time for each of the components described allowing an approximate estimate to be made for total build time.

Appendix C: Retrospective Risk Assessment Analysis

The risk assessment produced at the beginning of the project was followed and the project proceeded without incident. In addition to the mitigations discussed in the risk assessment the flying test bed controls were mounted to the outside of the test environment to ensure anyone controlling the flying test bed had full and unrestricted view of the vehicle in case of emergency.

Appendix D: ESDU 75026: Static Pressure Recovery Coefficient for Symmetric Annular Diffusers Without Tailpipes

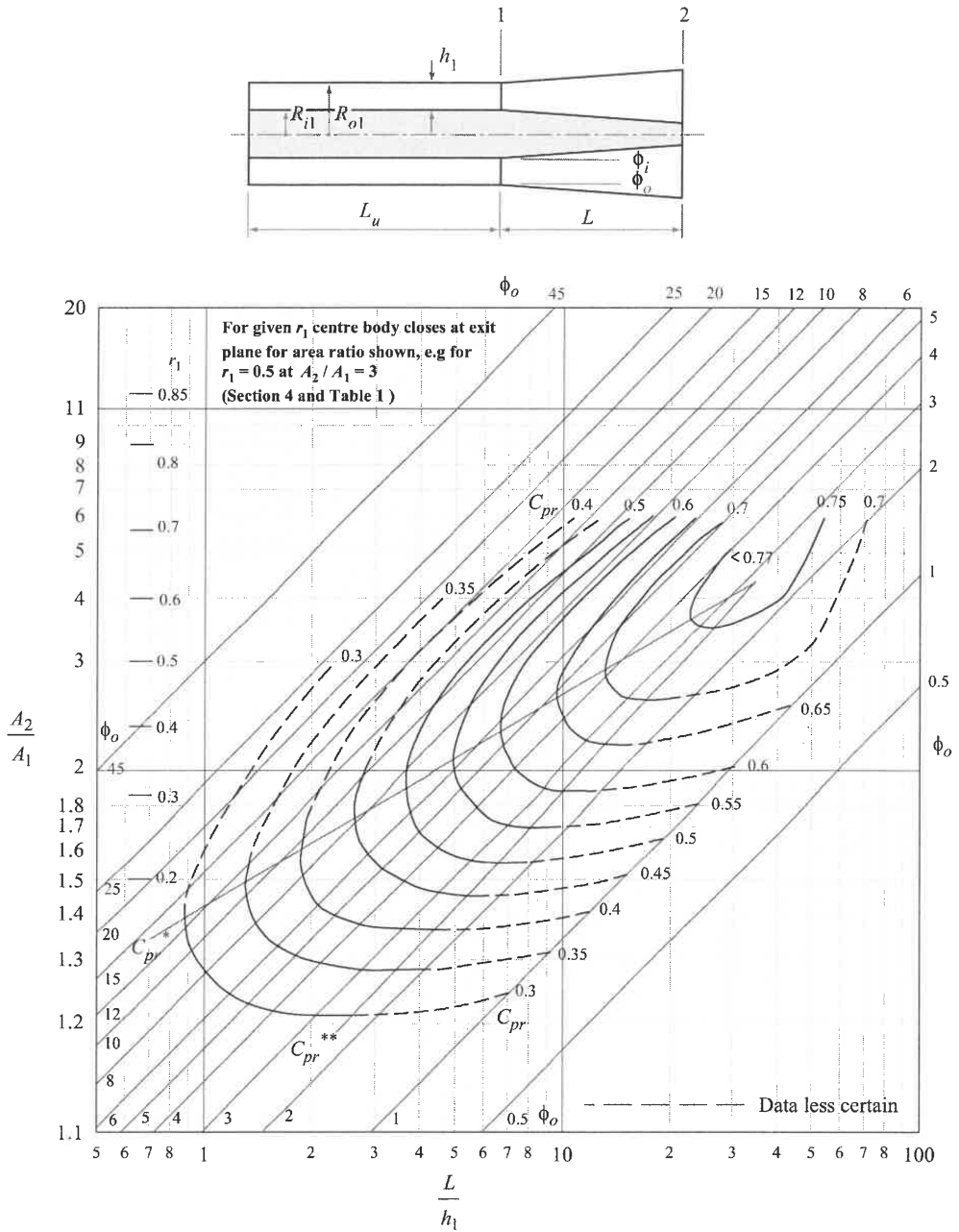


Figure 32: Static-pressure recovery coefficient, symmetrical annular diffusers without tailpipes and with fully developed entry flow, $L_u/h_1 \geq 100$